

Characterization and Modeling of a Control Moment Gyroscope

THESIS

2d Lt, Dylan Penn, B.S. AFIT-ENY-MS-15-M-235

DEPARTMENT OF THE AIR FORCE AIR UNIVERSITY

AIR FORCE INSTITUTE OF TECHNOLOGY

Wright-Patterson Air Force Base, Ohio

DISTRIBUTION STATEMENT A APPROVED FOR PUBLIC RELEASE; DISTRIBUTION UNLIMITED.



THESIS

Presented to the Faculty

Department of Aeronautical and Astronautical Engineering

Graduate School of Engineering and Management

Air Force Institute of Technology

Air University

Air Education and Training Command in Partial Fulfillment of the Requirements for the Degree of Master of Science in Astronautical Engineering

2d Lt, Dylan Penn, B.S., B.S. Mechanical Engineering

March 2015

DISTRIBUTION STATEMENT A APPROVED FOR PUBLIC RELEASE; DISTRIBUTION UNLIMITED.

CHARACTERIZATION AND MODELING OF A CONTROL MOMENT ${\bf GYROSCOPE}$

THESIS

2d Lt, Dylan Penn, B.S., B.S. Mechanical Engineering

Committee Membership:

Dr. Eric Swenson Chair

Dr. Richard Cobb Member

Dr. Frederick Leve Member

Abstract

The Air Force Research Laboratory (AFRL) is developing a spacecraft simulator that uses Control Moment Gyroscopes (CMGs). Prior to the research herin, the Air Force Institute of Technology (AFIT) designed and built six laboratory-rated CMGs for use on the AFRL spacecraft simulator. The main contributions of this research are in the testing and modeling of a single CMG.

Designing, building, and operating spacecraft simulators is time consuming and expensive, but less so than tests with on-orbit spacecraft. Reductions in cost and schedule can be realized by investing in modeling the spacecraft simulator and payload before testing. A model of the spacecraft simulator was created in previous research efforts, but was an ideal model; it did not include dynamics based on real CMGs. The objective of this research is to characterize and model a single CMG to determine the effects the real CMG's performance will have on the performance of the AFRL spacecraft simulator.

The gimbal motor utilizes a planetary gearbox, which has gear lash of 5°. Gear lash makes the existence of gravitational disturbance torques noticeable in the gimbal angular position measurements. An analytical model of the CMG gimbal was created in MATLAB. The model predicts the nonlinear dynamic behavior of the real CMG.

A model of the spacecraft simulator was run through a sequence of pointing commands to generate gimbal angle commands which were then used to command the CMG to evaluate the system's performance under realistic conditions. Gear slack has a cumulative time delay effect on vehicle slew responses of approximately one second over five maneuvers. The results of the tests performed in this thesis can be used to predict performance of CMG and spacecraft simulator behavior.

Acknowledgements

I would like to thank the following people for their contributions to this thesis effort:

Dr. Eric Swenson

Dr. Richard Cobb

Dr. Frederick Leve

Mr. Phillip Smith

Mr. Brian Crabtree and fellow machinists

Dr. Carl Hartsfield

Mr. James Herner

Mr. Sean Miller

2d Lt Dillon Simmons

Mr. Randall Sharp

Mr. Dominic DeSimio

Mr. Jorge Urena

Mr. Jay Anderson

Maj Cole Doupe

2d Lt, Dylan Penn, B.S.

Table of Contents

		Page
Abst	ract	iv
Ackr	owle	dgements
List	of Fi	gures viii
List	of Ta	ıbles xii
I.	Pro	olem Statement
	1.4 1.5 1.6	Introduction1Control Moment Gyroscopes (CMGs)2Spacecraft Simulators3Modeling4Objectives5Thesis Preview5Summary6
II.	Bac	kground7
	2.4	Introduction7Satellite Simulators7Control Moment Gyroscopes (CMGs)8Attitude Control Concepts92.4.1 Conservation of Angular Momentum92.4.2 CMG Equation of Motion10
	2.5 2.6 2.7	Gear Lash12Literature Review15Summary16
III.	Met	hodology
		Introduction 17 System Description 17 3.2.1 AFRL Spacecraft Simulator 18 3.2.2 AFIT CMG 18 3.2.3 CMG Control 20 3.2.4 Sensors 23
	3.3 3.4	Statistical Formulas24Testing253.4.1 Sensor Filtering263.4.2 Gimbal Balancing303.4.3 Sensor Noise33

			Page
	3.5	3.4.4 PID Control 3.4.5 CMG Model Validation 3.4.6 Simulated Maneuver 3.4.7 Vehicle-Level Model Summary	35 41 43
IV.	Res	lts	48
	4.3 4.4 4.5 4.6 4.7 4.8	Introduction Sensor Filtering Test Gimbal Balancing Test Sensor Noise Test PID Control Test From Hardware to Models CMG Model Validation Test 4.7.1 CMG Model Validation Test Results 4.7.2 Initial Analysis 4.7.3 Model Tuning 4.7.4 CMG Model Validation Test Conclusions Simulated Maneuver Test 4.8.1 Simulated Maneuver Test Results 4.8.2 Simulated Maneuver Test Analysis 4.8.3 Simulated Maneuver Test Conclusions Vehicle-Level Model Test 4.9.1 Vehicle-Level Model Test Results 4.9.2 Vehicle-Level Model Test Analysis 4.9.3 Vehicle-Level Model Test Conclusions Summary	48 56 58 67 67 67 74 75 76 79 80 80 83 90
V.		elusion	
v .	5.1 5.2	Introduction Conclusions 5.2.1 Hardware 5.2.2 Models Recommendations for Future Work 5.3.1 Hardware 5.3.2 Models	92 92 93 95 95
Арр	endix	A. Derivation of CMG Equations of Motion	98
	1.1	Spacecraft Dynamics	98

List of Figures

Figure	Page
1	AFIT's SimSat satellite simulator
2	AFIT CMG with major components labeled
3	CMG coordinate frame
4	Illustration of gear lash
5	Excess gear center distance causes gaps between mating teeth [30]
6	Illustration of planetary gear train center distance adjustment issue [30]
7	AFRL spacecraft simulator with CMGs mounted [28]
8	Exploded section view of the rotor housing subassembly19
9	Gimbal angle coordinate frame
10	Examples of gimbal angle measurements for CCW and CW rotations
11	Gimbal encoder [1]
12	CMG control flow diagram (single CMG)
13	AC3 box assembly (lid removed)
14	AC3 box attached to CMG
15	Hardware test setup diagram [1, 10, 25]
16	Two-point derivative flowchart
17	Five-point derivative with rollover correction flowchart
18	Representation of roll-over correction function
19	Electrical connector causing imbalance along gimbal axis
20	Diagram of gimbal imbalance looking along gimbal axis

Figure		Page
21	Temporary tunable mass balance installed on rotor housing	32
22	Free body diagram of gimbal forces	36
23	Input torque calculated from discrete velocity data (unfiltered)	37
24	gearlash function flowchart	38
25	CMG model flowchart	40
26	Example of gear lash function with a deadband width of 0.4 rad (23°)	41
27	Animated representation of spacecraft simulator output by MATLAB model	42
28	Command history for CMG # 1 from the spacecraft simulation	43
29	Block diagram of original spacecraft simulator model	45
30	Block diagram of spacecraft simulator model with gear lash	46
31	Velocity estimates from the sensor noise filter test	50
32	Full-length Kalman filter velocity estimates overlaid with encoder raw position measurements	51
33	Old (live) and new (post-processed) five-point derivative filter	52
34	Lowpass filter with two-point derivative filter as input (1st order, cutoff frequency=0.5 Hz)	53
35	Histograms of the filtered velocity measurements	54
36	Velocity step response with and without tunable mass balance	57
37	Gimbal balance test histogram (upper plot is CCW, lower plot is CW)	58

Figure	Page
38	The adjustable gimbal balance concept design allows for radial and axial movement, as shown in the center graphic
39	Sensor noise test data
40	Skewness for sensor noise test
41	First-order polynomial fit to experimental data
42	Step command test results from varying K_P $(K_I = 0, K_D = 0) \dots 64$
43	Step command test results from varying K_I $(K_P = 1, K_D = 0)$
44	Step command test results from varying K_D $(K_P = 1, K_I = 0)$
45	Step response metrics for variations in K_I ($K_P = 1$, $K_D = 0$)
46	The error derivative term dominates over the proportional term, causing instability $(K_D = 0.25, K_P = 1, K_I = 0) \dots 66$
47	Gimbal velocity sinusoid command test results
48	Diagram of signal sources for CMG model validation test [1]
49	Experimental and modeled gimbal results given identical input signal
50	Optimizing RMS error by varying K
51	Peak-to-peak time determining initial guess for time shift
52	Model versus experimental results with tuned design variables
53	Gears disengage at A, then reengage at B
54	Uncontrolled versus PI control results for CMG # 1 $(K_P = 1.1, K_I = 0.75)$
55	Uncontrolled versus modeled results for CMG # 1

Figure	Page
56	Individual components of controller inputs for CMG $\#$ 1
57	CMG model responds to command amplitudes more accurately than real CMG
58	Simulated gimbal and motor angles with 0° gear lash
59	Simulated gimbal and motor angles with 5° gear lash
60	Simulated gimbal and motor angles with 10° gear lash
61	Zoomed in simulated gimbal and motor angle data for all tests
62	Angular momentum from new spacecraft model simulation (5° gear lash, 20 Hz sample frequency)
63	Controller sampling frequency effects on angular momentum (5° gear lash)
64	Old spacecraft simulator model angular momentum results with same maneuver commands as new model test (no gear lash, 20 Hz sample frequency)
65	Pointing error for all tests89
66	CMG with rotor and gimbal axes
67	CMG with body frame

List of Tables

Table	Page
1	Sensor noise test setup parameters
2	Gains evaluated for PID control test
3	Standard deviation and RMS of filter data
4	Percent data points within 1- σ
5	Standard deviation of gimbal balance test data
6	Standard deviation (σ) , percent within 1σ (PW1 σ), and skewness of sensor noise test data
7	Minimizing function bounds and initial conditions
8	Model tuning results
9	Standard deviation of model versus real test data
10	Median of individual controller component terms for all CMGs
11	Changes in total angular momentum from beginning to end of simulations (no gear lash in old model, 5° gear lash in new model)
12	Time to complete each maneuver (maneuver complete when error $< 0.1^{\circ}$)
13	Overall simulation time when maneuver was completed (maneuver complete when error $< 0.1^{\circ}$)90

CHARACTERIZATION AND MODELING OF A CONTROL MOMENT GYROSCOPE

I. Problem Statement

1.1 Introduction

Spacecraft attitude control can be accomplished through various means; one of these is control moment gyroscopes (CMGs). Developing CMGs is technically challenging because it requires in-depth knowledge of mechanical, electrical, software, and control systems and the ability to design, build, and test hardware and software. The Air Force Institute of Technology (AFIT) is developing six CMGs for use on a large spacecraft simulator, which requires characterizing and modeling the CMGs. The spacecraft simulator allows control algorithms and spacecraft hardware to be tested in a lab setting. Most hardware-focused research on CMGs is proprietary; therefore detailed, publicly available literature on CMG hardware development is rare. This research represents one of the first openly-published modeling efforts of a single gimbal CMG.

This chapter presents the significance of CMGs and the motivation for this research effort. First, background on CMGs and spacecraft simulators is presented. Second, modeling concepts are examined, including motivation for modeling the CMGs. Third, the objectives of this research effort are outlined. Last, an overview of the thesis will be given, along with concluding comments.

1.2 Control Moment Gyroscopes (CMGs)

Whether it is to aim a camera, point an antenna, or maintain a desired slew rate, most spacecraft have a requirement to control their attitude. Consequently, the attitude control system (ACS) is a critical subsystem for most satellites. CMGs are momentum exchange devices used to slew spacecraft without the use of external torques. A CMG consists of a rotor disk that spins at a relatively fast constant speed on one axis and the gimbal, which rotates the rotor subassembly at a much lower rate along a perpendicular axis. CMGs exchange angular momentum with the spacecraft, resulting in a change in attitude of the spacecraft.

Mechanically, CMGs are complex and costly to design, build, and test. Because of the constant high rotor rotation rates and nominal spacecraft lifetime requirements of ten years or longer, rotor bearing performance is a critical design element [13, 26, 41]. The types of lubricants that can be used to combat bearing wear are highly limited due to outgassing requirements typical of the space environment [27]. Rotor alignment is also critical because even the slightest misalignment will cause increased bearing wear, jitter, over-heating, and loss of control precision, all of which can lead to catastrophic bearing failure resulting in partial or total loss of control authority and possibly the spacecraft [41]. Another significant challenge in CMG design is modeling the dynamic behavior of a CMG. Much research has been performed in modeling the effects of various CMG array configurations [2, 11, 19, 32]. However, there is little to no published research in modeling non-ideal single CMGs to the best of this author's knowledge. Due to the high development and quality assurance costs, very few companies produce CMGs, and of them, Honeywell Corporation is the only current company building CMGs for large spacecraft [21, 31]. Such companies do not make readily available their design approaches or analytical modeling techniques due to their proprietary nature. This research changes that paradigm.

1.3 Spacecraft Simulators

Testing spacecraft attitude control algorithms is generally impractical on-orbit because the mission sponsor typically will not accept the risk. Conversely, not all spacecraft dynamics can be readily simulated or the computer simulation results adequately trusted. This lack in reliable models is particularly true of not-well-characterized physical mechanisms, such as structural flexing or fluid slosh. Spacecraft simulators¹ are a hardware solution that offer an intermediate step between simulations and onorbit testing. Most spacecraft simulators emulate the space environment by allowing a test platform to rotate on a spherical air bearing. An air bearing has so little friction that the test platform experiences little to no rotational drag. Other styles of spacecraft simulators, such as air table simulators, do not utilize spherical air bearings, but are outside the scope of this research [33]. The test platform of a spacecraft simulator is a structure that allows various experimental payloads to be mounted to it. The test platform is equipped with its own ACS. In addition to testing control algorithms, spacecraft simulators are also used to test hardware. Spacecraft simulators have been developed and used successfully by the AFIT, the Naval Postgraduate School, NASA, Honeywell Corporation, and various research universities [33].

The Air Force Research Laboratory (AFRL) is developing a spacecraft simulator that utilizes CMGs. Because the AFRL spacecraft simulator is a laboratory test bed, buying space-rated CMGs would be significantly more expensive than is necessary. Therefore, AFIT designed and built six laboratory-rated CMGs for AFRL prior to this presented research effort. The main contributions of this research are in the testing and modeling of a single CMG. By designing the CMGs within the Air Force, as opposed to buying them from a company such as Honeywell, AFRL is saving

¹ "Simulator" is a slight misnomer within the field. A more accurate term would be "emulator", but is not used in literature.

a significant amount of money, as well as furthering Air Force knowledge of CMG development.

1.4 Modeling

Even though spacecraft hardware simulators can result in a significant cost and risk savings compared to on-orbit testing, operating them is still time consuming and expensive. In addition to the development cost of designing and building the test beds, skilled technicians are required to setup and run tests. Test setup is nontrivial and can typically take more time than the tests themselves. Consequently, further reductions in cost and schedule can be realized by investing in modeling the spacecraft simulator and payload before testing. Even if aspects of the test are difficult to model, such as fluid slosh, time can be saved by modeling the better-known aspects. The modeling process starts with creating an analytical model of the spacecraft simulator without a payload.

Because the AFRL spacecraft simulator's primary attitude control components are six CMGs, modeling these CMGs is critical in predicting performance of the whole test vehicle. A model of the whole vehicle was created in previous research efforts, but was an ideal model; it did not include dynamics based on the real CMGs [17]. Although such a model is applicable for the CMG design stage, allowing performance predictions by varying CMG geometry, mass, and size, it is not as accurate in predicting performance of real hardware. Now that the CMGs have been designed and built, their impact on the performance of the AFRL spacecraft simulator can be evaluated. The AFRL spacecraft simulator is still under development, therefore evaluating the CMGs through testing alone is not possible. At this stage of development, the presented research is focused on a combination of testing and modeling to characterize the CMGs' performance.

The performance characteristics of the CMG behavior were not well-known when it was built. Aspects of the CMG such as gimbal measurement noise, rotor measurement noise, motor position control accuracy, motor velocity control accuracy, and gear lash all have impacts on CMG (and vehicle) performance. In this research, these real factors are characterized to predict how and to what extent they impact the performance of the AFRL spacecraft simulator. After the various imperfections of reality in the CMG have been characterized, they can be modeled and incorporated into the higher-level vehicle model.

1.5 Objectives

Although the analytical dynamics of CMGs are well-documented, single CMG models are not currently matched to existing hardware and incorporated into whole-vehicle simulations [6, 17, 32]. If the attitude control performance of the AFRL space-craft simulator is to be well-understood to a high fidelity through simulation, a model of the non-ideal CMGs must be created and critically evaluated. The objective of this research is to characterize and model a single CMG to determine the effects it will have on the performance of the AFRL spacecraft simulator.

1.6 Thesis Preview

In the following chapters, the thesis objective is investigated through background investigation, testing, and analysis. Chapter II details CMGs, spacecraft simulators, and introduces attitude control concepts needed to understand the testing methodology. Gear lash, which is a critical mechanism of the real CMG, is also introduced. Chapter II concludes with a literature review of previous CMG research. Chapter III begins with descriptions of the spacecraft simulator and CMG, including details of the control hardware and software. The second half of Chapter III describes the ob-

jectives, methodology, and procedures for each test performed on the CMG. Chapter IV discusses the test results and analysis of each test. Finally, Chapter V provides an overview of the conclusions from the research and includes recommendations for further work into the subject.

1.7 Summary

Chapter I presented a brief background on CMGs, spacecraft simulators, and the motivation for modeling them. The objectives of the thesis were defined and an outline of the thesis was presented. Chapter II presents a more detailed background on CMGs, spacecraft simulators, and the mathematical concepts that govern attitude control.

II. Background

2.1 Introduction

CMGs are used for attitude control in spacecraft such as the International Space Station and the series of WorldView satellites [9, 15]. Satellite simulators are used to test attitude control hardware and software, including CMGs. This chapter presents the theoretical background of satellite simulators, CMGs, and spacecraft attitude dynamics. Gear lash¹, which is a specific concern in this research, is also discussed. Last, a literature review of related research is presented.

2.2 Satellite Simulators

Testing spacecraft attitude control hardware and algorithms together is difficult to perform in a lab setting because spacecraft are designed to operate in an torque free environment. On Earth, gravity induces external torques on the spacecraft, making it difficult to test spacecraft attitude control systems. Simulations are sometimes impractical or very challenging to model. In many cases, the dynamics of a satellite with flexing structures or fluid sloshing are not fully understood and can be difficult to model until a test is performed [33]. In these complex systems, testing can be performed on experimental satellite simulators (a.k.a. spacecraft simulators) in order to obtain data which can verify a dynamical model. Many types of satellite simulators allow for freedom in rotational motion, translational motion, or both. This research focuses on characterizing and modeling a CMG for use on a rotational spherical air bearing simulator, as seen in Figure 1. Spherical air bearing satellite simulators generally take the form of a test platform balanced on a hemispherical air bearing,

¹Gear lash, also called lash, backlash, play, or slack, is the lost motion in a mechanical gear train due to space between gear mating surfaces.

allowing for limited three axis rotational motion with near-zero friction forces acting at the bearing surface. Bearing size and mass capacity can range from 6-23 inches in diameter, and 450-20,3000 lbs, respectively [5]. Control actuators, such as reaction wheels, CMGs, and fans, are mounted on the test platform. A comprehensive, ableit dated, review of satellite simulators can be found in Schwartz et al. [33].

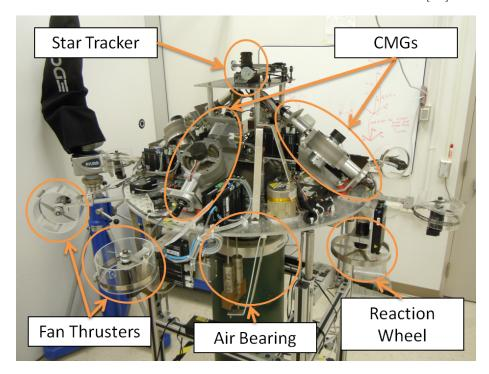


Figure 1. AFIT's SimSat satellite simulator

2.3 Control Moment Gyroscopes (CMGs)

A CMG consists of two components: a rotor and a gimbal. The rotor spins on a single axis at a constant rate. The gimbal rotates the rotor along a perpendicular (to the rotor spin axis) axis at a controlled rate in order to alter the direction and magnitude of the spacecraft body's angular momentum (Figure 2). The rotor generally rotates very rapidly (in the thousands of RPM), while gimbal rates are comparatively slow (in the single digits of °/sec). In a single gimbal CMG, the rotor spins at a constant rate along one axis (the rotor axis), while the rate of spin around a second

axis (the gimbal axis) is controlled. Double gimbal CMGs add a second controlled axis, but are less frequently used due to their complexity, and are not the focus of this research [15, 17]. CMGs are advantageous over reaction wheels because CMGs provide an "amplification" in output to input torque. This "amplification" in torque is caused because the output torques are created through velocities in the gimbal as opposed to accelerations, which would require shaft drive power. This is particularly useful on large spacecraft, which need larger internal torques to change attitude. However, CMG hardware and software are more complex than reaction wheels, requiring more robust testing and driving costs higher.

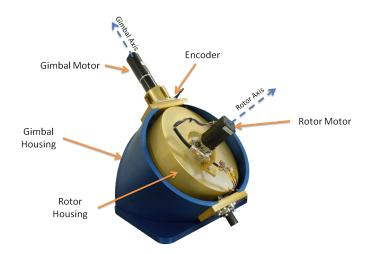


Figure 2. AFIT CMG with major components labeled

2.4 Attitude Control Concepts

2.4.1 Conservation of Angular Momentum.

The principal of conservation of angular momentum states that a system will maintain a constant total angular momentum unless acted upon by an external torque. When creating analytical models, control engineers tend to separate the spacecraft into two main components: the spacecraft body (the structure, and all non-moving

parts) and the control actuators. Assuming no external torques, the sums of the angular momentum of the spacecraft body and the control actuators must remain constant. Therefore, if a component such as a reaction wheel accelerates, the spacecraft body must react by accelerating in a direction correlating to the mounting angle of the wheel relative to the spacecraft body frame and with magnitude proportional to the ratio of the wheel and spacecraft's moment of inertia (MOI) about the wheel's spin axis. This mechanism is called exchange of angular momentum, and is mathematically described as

$$\vec{H}_{SC} = I_{sc}\vec{\omega}_{sc} + \vec{h}_{actuators} \tag{1}$$

where \vec{H} and \vec{h} are angular momentum, I is MOI, $\vec{\omega}$ is angular velocity, and "SC" denotes spacecraft [37].

2.4.2 CMG Equation of Motion.

The expression for the angular momentum of a CMG in the body frame is

$$\vec{h}^b = R_3^T(\theta) \begin{bmatrix} I_g c \beta \dot{\delta} + I_r \Omega s \beta c \delta \\ -I_r \Omega s \delta \\ -I_g s \beta \dot{\delta} + I_r \Omega c \beta c \delta \end{bmatrix}$$
(2)

where s and c denote the sine and cosine functions, respectively, R_3 is the rotation matrix about the 3-axis, I_g is the MOI of the CMG along the gimbal axis, I_r is the MOI of the rotor along the rotor axis, δ is the gimbal angle, and Ω is the rotor angular velocity. The symbol θ is the planar angle between the spacecraft frame and CMG frame, shown in Figure 3. The symbol β is the off-planar angle (skew angle) between the spacecraft frame and CMG frame, also shown in Figure 3.

The derivation of Eq. (2) is covered in many sources, including Appendix A of

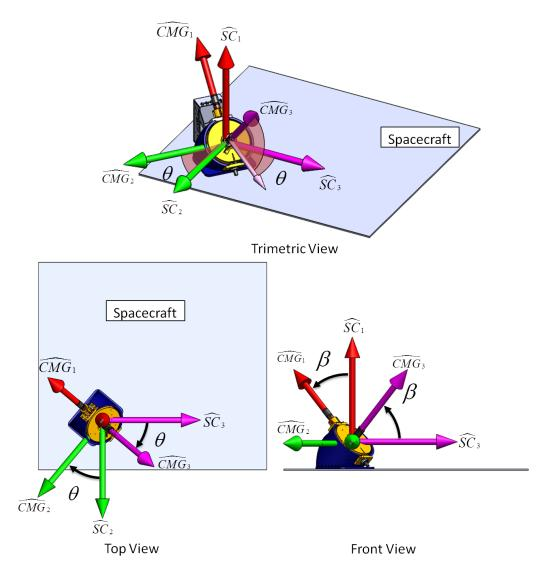


Figure 3. CMG coordinate frame

this thesis [11, 17, 19]. The angular momentum of a spacecraft controlled by n-CMGs can be written as

$$\vec{H} = I\vec{\omega} + \sum_{j=1}^{n} \vec{h}_j \tag{3}$$

where I is the MOI of the spacecraft body. The inertial time-derivative of Eq. (3) is shown in Eq. (4) which is the governing equation for the kinetics of a spacecraft controlled by a CMG array. Note that Eq. (3) has omitted terms relating to the

angular momentum of the gimbal by assuming that the rotor angular rate is much greater than both the gimbal rate and acceleration [11, 17, 19].

$$\dot{\vec{H}} = I\dot{\vec{\omega}} + \sum_{j=1}^{n} R_3^T(\theta_j) \begin{bmatrix} -I_r \Omega_j s \beta s \delta_j \dot{\delta}_j \\ -I_r \Omega_j c \delta_j \dot{\delta}_j \\ -I_r \Omega_j c \beta s \delta_j \dot{\delta}_j \end{bmatrix} + \vec{\omega} \times I\vec{\omega} + \vec{\omega} \times \sum_{j=1}^{n} R_3^T(\theta_j) \begin{bmatrix} I_r \Omega_j s \beta c \delta_j \\ -I_r \Omega_j s \delta_j \\ I_r \Omega_j c \beta c \delta_j \end{bmatrix} \tag{4}$$

A specific case of Eq. 4 is shown in Eq. 5, which describes the angular momentum of a spacecraft with a four-CMG array in a pyramid configuration [17]. Eq. 5 is used in the spacecraft simulator model described in Sections 3.4.6 and 3.4.7. In Eq. 5, $\bar{\delta}$ denotes the vector of CMG gimbal angular rates.

$$\dot{\vec{H}} = I\dot{\vec{\omega}} + I_r\Omega \begin{bmatrix}
-s\beta c\delta_1 & s\delta_2 & s\beta c\delta_3 & -s\delta_4 \\
s\delta_1 & s\beta c\delta_2 & -s\delta_3 & -s\beta c\delta_4 \\
c\beta c\delta_1 & c\beta c\delta_2 & c\beta c\delta_3 & c\beta c\delta_4
\end{bmatrix} \dot{\vec{\delta}} + \begin{bmatrix}
-s\beta s\delta_1 & -c\delta_2 & s\beta s\delta_3 & c\delta_4 \\
-c\delta_1 & s\beta s\delta_2 & c\delta_3 & -s\beta s\delta_4 \\
c\beta s\delta_1 & c\beta s\delta_2 & c\beta s\delta_3 & c\beta s\delta_4
\end{bmatrix} (5)$$

2.5 Gear Lash

The AFIT CMG gimbal motors are comprised of two components: a high-speed DC motor and a triple reduction gearbox. The motor is a high-speed, low-torque model, therefore the gearbox is necessary to step the speed down and the torque up. The gearbox has three planetary gear trains, with a total gear ratio of 116 [3].

In a gear train, the mechanism whereby gaps between teeth cause a gear to rotate at a different rate than its mating gear is known as gear lash, gear slack, or backlash [7]. This difference presents itself whenever the driven gear is allowed to lose contact with the driving gear, such as during a direction change. This process is illustrated in Figure 4.

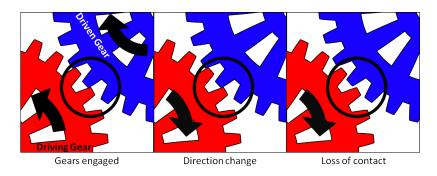


Figure 4. Illustration of gear lash

Gear lash can be caused by, among other sources, uneven teeth wear, poor lubrication, imprecise machining tolerances, or excessive gear center distance. The pertinent cause of gear lash for this research is gear center distance. When the planet gear teeth become too far away from either the ring or sun gear, the teeth do not fully mesh, causing gaps to appear between the surfaces of the gear teeth (Figure 5). Because the CMG gimbal motor has three planetary gear trains, there are three points of gear lash in the system.

A common solution to gear lash is to decrease the distance between the gear centers either by manual adjustment or a spring mechanism that draws the gears together with a constant force [29]. However, in planetary gear trains, decreasing the spacing between a sun and a planet gear causes the distance between the planet and ring gear to increase, as shown in Figure 6. The opposite happens if the distance between the planet and ring gear is decreased. Therefore, planetary gear trains are inherently susceptible to gear lash [36].

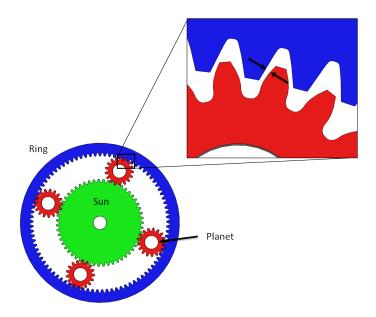


Figure 5. Excess gear center distance causes gaps between mating teeth [30]

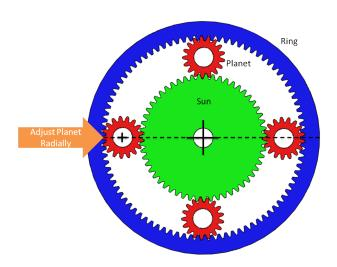


Figure 6. Illustration of planetary gear train center distance adjustment issue [30]

2.6 Literature Review

This research is a follow-on of research conducted by Johnson [17], which investigated design methodology for a CMG. Johnson's work focused on CMG design which required him to derive component-level (CMG) requirements and performance envelopes from vehicle level requirements. He modified an existing analytical model of the AFRL spacecraft simulator and utilized it to size the CMG rotor and motors. A later version of this analytical model was utilized in this thesis. A prototype CMG was designed using Computer-Aided Drafting (CAD) tools as well as trade studies for the motors, bearings, and gimbal encoder. A performance comparison was made between the AFIT CMG and the Honeywell M50, a commercially available space-rated CMG [21]. Singularity surfaces for pyramid and rooftop CMG array configurations were calculated. A prototype CMG was built and preliminary tests performed. The CMG developed in Johnson's work is not the same CMG used in this research, as the prototype CMG was later redesigned.

Most CMG research focuses on vehicle-level design, particularly regarding CMG array configurations [2, 11, 19, 32]. When controlling a spacecraft with CMGs, the sum of the angular momentum of the CMGs must be "steered" to orient the spacecraft. The angular momentum vector of the CMG array must always travel within a three-dimensional volume in momentum space. This surface enclosing the volume is known as the momentum envelope, or singularity surface, of the array. The spacecraft cannot be commanded to provide all desired torques when its angular momentum vector is on a singularity surface. Much research has been performed on the subject of singularity surface calculation and avoidance [2, 11, 19, 32].

Most operational CMGs have a fixed-speed rotor; however, there is much research into theoretical variable-speed CMGs (VSCMGs) [24, 42]. VSCMGs are advantageous over fixed-speed CMGs because the variable-speed rotor eliminates most singularities.

Research has been performed which utilizes VSCMGs as both control actuators and power storage devices [42]. The basic concept behind VSCMGs as power control systems is that, by despinning a rotor, the kinetic energy can be transferred to electrical energy for use in other spacecraft subsystems. VSCMGs are still theoretical, and are out of scope for this research.

2.7 Summary

Chapter II presented background on satellite simulators, CMGs, and the mathematical concepts that govern them. The concept of gear lash was introduced. Last, a review of other relevant research in the field of CMGs was presented. Chapter III brings to reality topics from Chapter II by detailing the spacecraft simulator and its AFIT-designed CMG as well as the control hardware and software for the CMG. Chapter III then outlines the test methodology and procedures utilized to characterize and evaluate the CMG.

III. Methodology

3.1 Introduction

The focus of this thesis is on modeling the AFIT CMG and its effects on the space-craft simulator performance. The CMG has been designed and built, but not analytically characterized. To create a representative analytical model of the CMG, the system must first be characterized with respect to measurement noise and open-loop behavior. This chapter presents the methods by which the CMG was characterized and modeled.

This chapter details the CMG that this research investigates and the analyses thereof. In Section 3.2, the AFRL spacecraft simulator is examined, followed by the physical components of the CMG. The control system of the CMG is detailed, including both the hardware and software components of the communication network. Section 3.4 details the various tests performed to characterize the CMG, in which test motivations, objectives, and procedures are discussed. There are seven tests, divided into two categories: hardware and modeling. The hardware tests (Sections 3.4.1 through 3.4.4) evaluate characteristics of the real CMG. The modeling tests (Sections 3.4.5 through 3.4.7) present the development of the CMG and spacecraft simulator models.

3.2 System Description

The hardware of interest for this research is the CMG developed by AFIT for use on the AFRL spacecraft simulator. The CMG array includes all the electronic hardware necessary to control each CMG. This section describes the overall spacecraft simulator and how it interfaces with the CMG array, the mechanical and electrical CMG components, and the CMG control hardware and software.

3.2.1 AFRL Spacecraft Simulator.

The spacecraft simulator is a rotational spherical air bearing satellite simulator developed by the AFRL Space Vehicles Directorate for use in testing satellite control algorithms (Figure 7) [28]. The simulator is equipped with different types of attitude determination and control hardware, including reaction wheels, CMGs, rate gyroscopes, and compressed air thrusters. In order to isolate the test platform from external torques, wires cannot connect the external environment to the components. Therefore, the simulator is battery powered and all communication to the test platform is performed via a wi-fi connection. The spacecraft simulator is designed to have six CMGs mounted to it in a rooftop configuration, but operators may not necessarily use all of them simultaneously [17].



Figure 7. AFRL spacecraft simulator with CMGs mounted [28]

3.2.2 AFIT CMG.

The AFIT CMG consists of two main subassemblies: the rotor housing and the gimbal housing (Figure 2). The rotor housing holds the rotor, a 21 pound (9.52 kg),

1 inch thick, 9.6 inch diameter, stainless steel disk (Figure 8). The rotor is mounted on two ABEC 1¹ ball bearings, which constrain the rotor in the radial and axial direction, leaving the rotation axis as the only free degree of freedom. The rotor drive shaft is connected to the rotor via a spring coupler, which allows for minor shaft misalignments in the axial, parallel, and angular directions [16]. The rotor is powered by a brushless DC motor rated to 557.9 mN-m (4.938 in-lbf) [4]. The motor has Hall effect sensors, which allows the rotor speed to be read directly from the motor. A counterweight is mounted to the rotor housing, opposite the motor, in order to balance the weight of the motor along the gimbal axis.

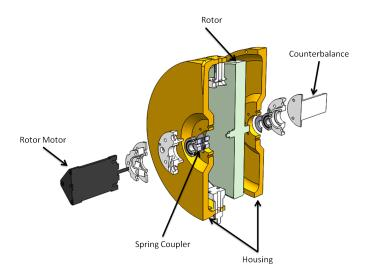


Figure 8. Exploded section view of the rotor housing subassembly

The CMG gimbal housing is cut from an aluminum straight pipe, within which the rotor housing subassembly rotates. The gimbal angle is controlled by a brushless DC motor with a gear box that steps up the torque to 14.71 N-m (130 in-lbf) [3]. Although the motor has built in Hall sensors, CMG control requires precision gimbal angle knowledge, which the sensors cannot achieve. Therefore, a magnetic ring encoder is mounted on the gimbal which is rated to a measurement accuracy of $\pm 0.1^{\circ}$ (Figure 11)

¹Annual Bearing Engineering Committee: A scale developed by the American Bearing Manufacturers Association to rate bearing precision. The scale ranges from one to nine, with the higher numbers denoting more precise tolerances [12].

[1]. The coordinate system utilized for the gimbal angle, shown in Figure 9, denotes counterclockwise (CCW) motion as positive and clockwise (CW) motion as negative. The gimble angle is measured from 0-359.9° (0- \sim 2 π rad). When the gimbal "rolls over" from a high angle to a low angle, or vice versa, the measured angle shows a sharp jump in value. The direction of this jump is shown in Figure 10 for both CCW and CW rotations.



Figure 9. Gimbal angle coordinate frame

The gimbal motor, rotor motor, and encoder wires all connect to the AFIT CMG CAN Controller (AC3) box, described in Section 3.2.3. All CMG controls are sent through the AC3.

3.2.3 CMG Control.

CMG control is accomplished through a variety of electrical and software components. The motors each connect to an off-the-shelf analog controller. In addition to these controllers, all communication is performed over the controller area network (CAN) bus. The analog controllers are connected to the AC3, an AFIT-developed

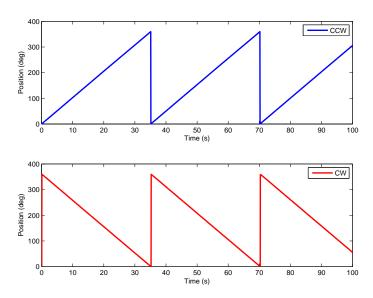


Figure 10. Examples of gimbal angle measurements for CCW and CW rotations



Figure 11. Gimbal encoder [1]

computer board, which is in turn connected to a dSPACE MicroAutobox II (MAB), which is in turn connected to a computer (Figure 12). This section details each component in the CMG control network, addressing each element in Figure 12.

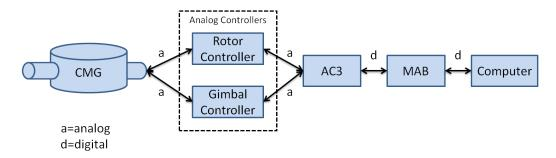


Figure 12. CMG control flow diagram (single CMG)

dSPACE MicroAutoBox II (MAB).

The MicroAutoBox II (MAB), manufactured by dSPACE Incorporated, interfaces between a computer and controller hardware. Functionally, the MAB is a field-programmable gate array² (FPGA) that allows engineers to rapidly change and test control algorithms. The MAB interfaces with MATLAB/Simulink, a common engineering software package which does not require the user to posses low-level coding knowledge. The MAB can interface with a variety of analog and digital devices over many different communication protocols, including the CAN bus [10].

Controller Area Network (CAN) Bus.

The CAN bus is a serial communication protocol, used commonly in the automotive industry, that allows more than two nodes to communicate with each other over the same set of wires [39]. Using CAN allows each node in a system to be individually programmed to "listen" for messages that contain a particular identifier or set of

²A FPGA is programmed by the user in the field (hence "field programmable"), as opposed to an application-specific integrated circuit (ASIC), which is programmed when the hardware is built in the factory.

identifiers. Each controller responds to a CAN message only if that message includes the assigned identifier(s).

AFIT CMG CAN Controller (AC3).

The AC3 is a custom computer board that interfaces between the MAB and the motor controllers. The AC3 converts signals between analog (from the motor controllers) and CAN (from the MAB). The AC3 is shown in Figure 13. Each AC3 connects with a rotor controller, a gimbal controller, and a position encoder. The AC3 board is housed in a box along with the two motor controllers; the box is attached to the back of the CMG (Figure 14).

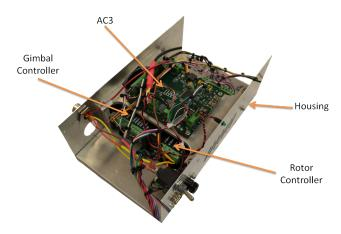


Figure 13. AC3 box assembly (lid removed)

3.2.4 Sensors.

The CMG hardware outputs three telemetry items of interest for analysis:

- Rotor speed via Hall sensors³ in the rotor motor
- Gimbal speed via Hall sensors in the gimbal motor

³Hall sensors (or Hall effect sensors) are magnetic sensors used in DC motors to measure angular rate. Each time the motor arms passes by a sensor, a magnetic pulse is formed. By positioning sensors with even angular spacing around the motor shaft, rotations can be measured by pulse timing [34].



Figure 14. AC3 box attached to CMG

• Gimbal position via the magnetic encoder ring

The position encoder is more accurate than the gimbal motor Hall sensor for position measurements and velocity measurements. The position encoder outputs a pulse-width modulation (PWM) signal, of which the pulse width corresponds to angular position, from 0°to 359.99451°, with a 16 bit resolution [1].

3.3 Statistical Formulas

Throughout the tests analysis conducted in this research, standard deviation σ , root mean squared RMS, and skewness S are used to statistically describe data sets. Eqs. 6, 7, and 8 shows the mathematical expressions of σ , RMS, and S, respectively. In Eqs. 6 to 8, \overline{x} is the mean of the data set and n is the length of the data set.

$$\sigma = \left(\frac{1}{n} \sum_{i=1}^{n} (x_i - \overline{x})^2\right)^{\frac{1}{2}} \tag{6}$$

$$RMS = \sqrt{\frac{1}{n} \left(\sum_{i=1}^{n} x_i^2\right)} \tag{7}$$

$$S = \frac{\frac{1}{n} \sum_{i=1}^{n} (x_i - \overline{x})^3}{\sigma^3} \tag{8}$$

In cases where RMS error is calculated, a modified version of Eq. 7 is used:

$$RMS = \sqrt{\frac{1}{n} \left(\sum_{i=1}^{n} (\hat{x}_i - x_i)^2\right)}$$

$$\tag{9}$$

where \hat{x} is the value x is being normalized to.

3.4 Testing

This section presents all of the methodology, background, and procedures for each test performed in this research. The tests can be divided into two groups: hardware and modeling. The hardware tests (sensor filtering, gimbal balancing, sensor noise, and PID control) concern characterizing the performance of the CMG. The modeling tests (CMG model validation, simulated maneuver, and vehicle-level model) concern creating and validating computer models of the CMG and the spacecraft simulator.

Figure 15 shows the test setup for all hardware tests. Note that the acceleration limit for the gimbal is 5 rad/s² and the velocity limit is 100°/s (1.745 rad/s). Unless otherwise specified, tests are performed with feedback control and a proportional gain of one. This is effectively running the CMG in an open-loop configuration. "True" open-loop tests cannot be run on the gimbal because without feedback the gimbal would accelerate at a constant rate until the fuse in the AC3 trips, cutting power to the CMG. Unless otherwise noted, the sampling rate for all tests is 20 Hz and are conducted with the rotor off (not spinning).

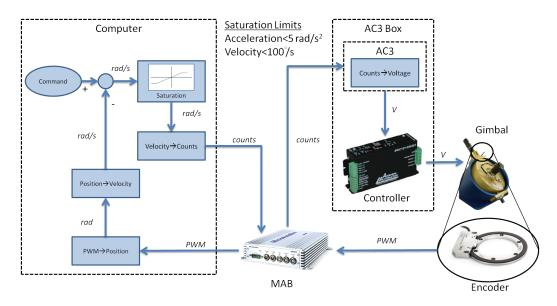


Figure 15. Hardware test setup diagram [1, 10, 25]

3.4.1 Sensor Filtering.

Sensor Filtering Test Introduction.

This section presents the descriptions of different filters utilized to estimate the gimbal angular velocity, followed by the sensor filtering test procedures. Commanding the gimbal velocity accurately is required to control the spacecraft simulator. The position encoder provides accurate angular velocity measurements to within 2°/sec, compared to the gimbal motor's built-in Hall sensor of approximately 8°/sec. However, differentiating position measurements in real-time to derive velocity results in noisy data. Three different filtering techniques are used to decrease measurement noise, described next [35, 40]. The objectives of the sensor filtering test are to:

- Characterize the performance of the 2-point derivative filter, 5-point derivative filter, Kalman filter, and Hall sensor measurements on gimbal velocity measurements.
- Determine which of the four measurement sources (three different filters and the Hall sensor) is most effective for continued use on the gimbal.

Filters.

The three different filters used for estimating velocity data are: two-point discrete derivative without roll-over correction, five-point discrete derivative averaging with roll-over correction, and a Kalman filter with roll-over correction. The filters are described in detail below.

2-Point Discrete Derivative The least complex of the filters, the two-point discrete derivative filter, illustrated in Figure 16, calculates the discrete derivative between two adjacent position measurements. There is a discontinuity when the raw position measurements from the encoder transition around the zero point, where one measurement is nearly 0° and the other is nearly 360°. This roll-over condition produces a large spike in velocity because the filter is taking the discrete derivative of two far separated values. The two-point filter does not use the roll-over correction function used in the five-point filter, described next, to observe the discontinuity in the estimates.

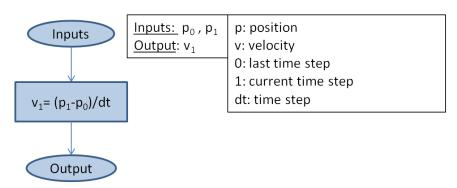


Figure 16. Two-point derivative flowchart

5-Point Derivative The five-point derivative filter, illustrated in Figure 17, is an enhanced version of the two-point filter. The five-point derivative filter calculates the discrete derivative of the five previously reported position values, totaling four velocity values, then reports the average of the velocities [35]. This filter

includes a roll-over correction function to account for the zero point discontinuity. When a large difference between any two of the five position measurements is detected, all high values (those near 360°) are offset by -360°. This roll-over correction process is shown in Figure 18. In Figure 18, five measurements are recorded, but because the measurements were taken during a roll-over event, the last data point, measurement number five, is far removed from the other four on the y-axis. Without roll-over correction, three small velocities and one large velocity would be calculated. With roll-over correction, the four higher values are offset by -360°. Velocity values are calculated from the offset data, resulting in four small velocities, which are then averaged to report a final velocity.

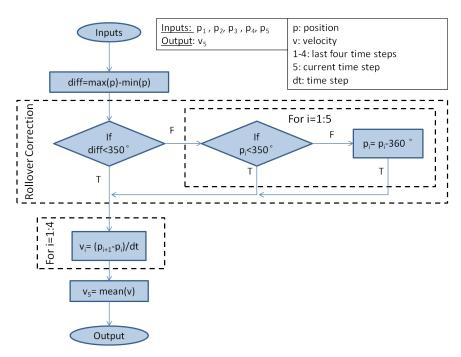


Figure 17. Five-point derivative with rollover correction flowchart

Kalman Filter The third filter tested is the Kalman filter. Theoretical background on Kalman filters is outlined in many sources [8, 18, 40]. The Kalman filter uses the previously described five-point derivative filtered velocity as its input

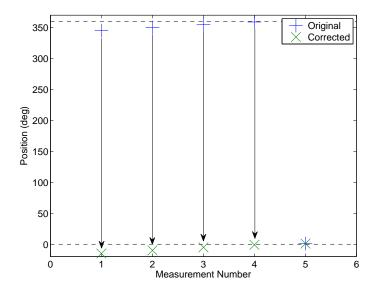


Figure 18. Representation of roll-over correction function

measurement. The state equations used in the Kalman filter are

$$\ddot{\delta} = [0]\dot{\delta} + [1/I_{qimbal}]T \tag{10a}$$

$$\dot{\delta} = [1]\dot{\delta} + [0]T. \tag{10b}$$

where $\dot{\delta}$ is angular velocity, $\ddot{\delta}$ is angular acceleration, I_{gimbal} is the MOI of the rotor assembly about the gimbal axis, and T is the commanded torque.

Sensor Filtering Test Procedures.

To characterize the different velocity filters, a constant velocity of 0.5 rad/s was commanded to the gimbal motor while position and velocity data were recorded for 120 seconds at 20 Hz sample frequency, for a total of 2400 data points per test. The angular velocity of 0.5 rad/s was chosen because it is a moderate velocity, less than one-third of the CMG's maximum operating velocity of 100°/s (1.745 rad/s). The long test duration allowed any transients in the system to subside and for the steady-state behavior of the system to be observed. This was repeated for both

positive (counter-clockwise) and negative (clockwise) directions in order to observe any direction-induced irregularities.

During the test, raw measurement data and filtered data were recorded. The Kalman filter-derived signal was fed back into the controller, but no active control (eg: PID) was used. This test took place after the gimbal axis was balanced (see Section 3.4.2).

3.4.2 Gimbal Balancing.

Gimbal Balancing Test Introduction.

The design of the rotor housing did not include a fine-tuning balancing mechanism. The electrical connections on one side of the rotor housing, shown in Figure 19, add an imbalance to the housing. The extra mass causes the rotor housing to have a preferred orientation, which impedes controllability of the CMG. The objective of the gimbal balancing test is to:

• Evaluate the effect on gimbal velocity measurements from installing a tunable mass balance on the rotor housing

Gear Lash.

The gimbal motor utilizes a planetary gearbox, which has inherent gear lash [36]. In the CMG gimbal, gear teeth contact is lost when the rotor housing center of mass, which is not aligned with the gimbal axis, transitions from one side of the center of rotation to another, as shown in Figure 20. The black circle in Figure 20 represents the imbalanced mass which induces an imbalance torque causing the gimbal to accelerate, thereby accelerating the driven gear in the motor. The acceleration causes the driven gear to briefly lose contact with the driving gear, resulting in an

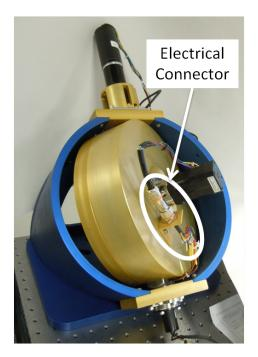


Figure 19. Electrical connector causing imbalance along gimbal axis

increase in gimbal velocity until the gear teeth reestablishes contact. The imbalance can be easily counteracted by adding trim mass to the rotor housing.

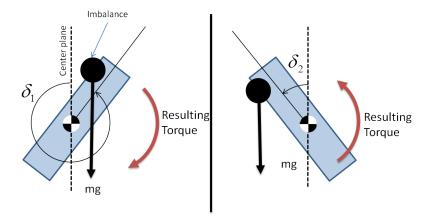


Figure 20. Diagram of gimbal imbalance looking along gimbal axis

Tunable Mass Balance.

Due to imperfections in machining, placement of fasteners, and the addition of wiring and connectors, it is impossible to create a perfectly balanced gimbal; therefore,

a tunable mass balance was built to install on the rotor housing. To create a mass balance, a tapped hole was drilled on the rotor housing cover plate, which is located opposite the electrical connector on the rotor housing. A threaded rod was fastened into the hole, allowing extra mass to be added to the rotor housing, as shown in Figure 21. The rotor housing was balanced by adding mass to the threaded rod until the housing no longer showed a preferred orientation. Masses of approximately 5g increments in the form of washers were utilized as trim mass. The total mass added to the housing was 181g.

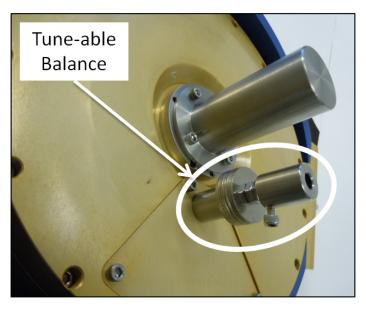


Figure 21. Temporary tunable mass balance installed on rotor housing

Gimbal Balancing Test Procedures.

To evaluate the effectiveness of the mass balance, the gimbal was tested with and without the balance. A step command of 0.5 rad/s was input for 300 seconds. This was repeated for both positive (counter-clockwise) and negative (clockwise) directions in order to observe any direction-induced irregularities, for a total of four tests. Position and velocity data were gathered during the test.

3.4.3 Sensor Noise.

Sensor Noise Test Introduction.

The gimbal balance test results (Section 4.3) show bias is measurements from the position encoder, which can be seen in Figure 37. However, the gimbal balance test was unable to determine the source of the sensor noise in the measured data. This section presents the sensor noise test methodology, which characterizes the measurement noise of the encoder-derived velocity measurements. Because all previous tests have observed the gimbal velocity at only a single value (0.5 or -0.5 rad/s), this test also provided the opportunity to characterize the system at a variety of velocities. The objectives of the sensor noise test are to:

- Determine if velocity measurement noise is similar over a range of velocities
- Determine if the gimbal operates linearly for steady-state velocity inputs

Sensor Noise Test Procedures.

The gimbal was commanded at a constant angular velocity and the Kalman filter estimated velocity data was recorded for 20 seconds, for a total of 400 data points per test. Nine tests were performed, each at a different commanded velocity, including zero. The test inputs are summarized in Table 1. This test was performed on the balanced gimbal (see Section 3.4.2), using Kalman filtered velocity estimates in the feedback loop.

3.4.4 PID Control.

PID Control Test Introduction.

In order to first characterize the system, all previous tests (sensor filtering, gimbal balancing, and sensor noise) were performed without closed-loop feedback control in

Table 1. Sensor noise test setup parameters

Parameter	Value
Commanded Velocity Range (rad/s)	-1 to 1
Commanded Velocity Step Size (rad/s)	0.25
Total # of Tests	9
Test Length (s)	20
# Data Points per Test	400

order to examine the performance of the open-loop system which gave the opportunity to study errors and noise that control may have counteracted. As a result, the gimbal did not achieve commanded velocities in previous tests. The PID control test investigates different values of proportional-integral-derivative (PID) control gains to characterize operating regions for a PID controller. The objectives of the PID control test are:

- Characterize the gimbal behavior with different PID gains when commanding velocity
- Determine ranges of PID gains to investigate for further gimbal tuning

PID Control Test Procedures.

The gimbal, starting from rest, was issued a velocity step command. Velocity data was recorded for 20 seconds. This test was repeated for a range of K_P (proportional), K_I (integral), and K_D (derivative) values, which are shown in Table 2. To isolate the effects caused by the controller, only one gain $(K_P, K_I, \text{ or } K_D)$ was adjusted at a time. A total of three tests were performed, with multiple (but not equal) numbers of runs per test. The gains chosen are separated by relatively large intervals to examine the system behavior over a wide operating range. Starting gain values were 0.25, and increased by 0.25 increments until either, a) the system became unstable, causing a test abort, or b) the system response stopped changing drastically between

increments.

Table 2. Gains evaluated for PID control test

Test #	Independent Gains	Dependent Gains
1	$K_I = 0, K_D = 0$	$K_P=1, 1.25, 1.5$
2	$K_P = 1, K_D = 0$	$K_I = 0.25, 0.5, 0.75, 1, 1.25, 1.5, 1.75, 2$
3	$K_P = 1, K_I = 0$	$K_D=0.25, 0.5$

3.4.5 CMG Model Validation.

CMG Model Validation Test Introduction.

This section presents the method and structure of the CMG gimbal model validation test. A single CMG model is developed to supplement the higher-level spacecraft model (developed by Swenson and Johnson). A model of the CMG will allow wholevehicle performance to be more accurately predicted in simulations. Additionally, a model may be used within the control loop of the CMG to further improve controllability. Therefore, it is desirable that the model be made with real-time incorporation in mind. However, before a model can be integrated into the control system, it must be validated by test data comparison. First, the structure of the model is outlined, followed by a comparison to test data. The objectives of the CMG model validation test are to:

- Create a model of the CMG that incorporates the effects of gear lash
- Create a model of the CMG that closely matches real test data

State Space.

The gimbal motor is modeled as a friction-less wheel with a torque input acting on it, as seen in Figure 22, where δ is gimbal angle, T is torque, and I is the MOI about the gimbal axis.

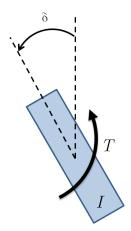


Figure 22. Free body diagram of gimbal forces

The state space representation of this model, using states of gimbal angle δ and gimbal angle rate $\dot{\delta}$, is

$$\dot{\overline{x}} = \begin{bmatrix} \dot{\delta} \\ \ddot{\delta} \end{bmatrix} = \begin{bmatrix} 0 & 1 \\ 0 & 0 \end{bmatrix} \begin{bmatrix} \delta \\ \dot{\delta} \end{bmatrix} + \begin{bmatrix} 0 \\ 1/I \end{bmatrix} T.$$
(11)

In order to use Eq. (11) two conditions must be met: 1) the commanded torque T must be known and 2) the MOI I must be known. To calculate the commanded torque in discrete, real time, we use

$$T = I \frac{\omega_1 - \omega_0}{dt} \tag{12}$$

where dt is the time step (0.05 sec), and the subscripts of ω denote discrete time values of the angular velocity. Due to inherent noise in the system, taking the discrete derivative of velocity to calculate acceleration, as in Eq. 12, results in a noisy torque value. Calculating the commanded torque in discrete time results in a noisy input signal into the state space model, which is not reflective of reality. An example of a discrete time torque signal is shown in Figure 23.

Noisy torque signals could be smoothed with a moving average method, such as

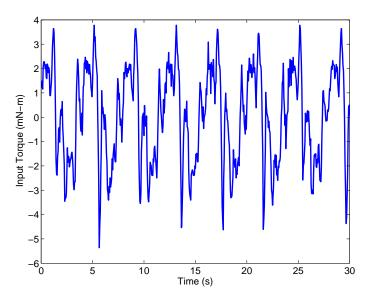


Figure 23. Input torque calculated from discrete velocity data (unfiltered)

that presented in Section 3.4.1, but would induce a lag into the model. The MOI can be estimated from CAD software; however, this does not account for the electrical connector on the side of the rotor housing (Figure 19). The position and lengths of the wires in the connection may be different from one CMG to another, changing the MOI from nominal, although not significantly. Therefore, the MOI would have to be calibrated in the model for each CMG. Of the two concerns, the noisy torque signal is the more difficult to work around.

An alternative method to using torque as the input signal for the model is to use the input velocity error as the input. The velocity error (a.k.a. velocity input, not to be confused with commanded velocity) is calculated in the Simulink model of the CMG and is not excessively noisy. By using velocity input v as the state space input, this allows for the 1/I term in Eq. (11) to be abstracted to an experimentally determined constant K. This new state space model is shown in Eq. (13). The overall CMG model is shown in Figure 25. The model uses as outer control loop to command gimbal velocities and an inner loop running ode45 to simulate the physics of the gimbal. The system contains nonlinearities that the state space model alone

does not capture. The dominant among these nonlinear terms is gear lash. Gear lash is incorporated into the model to closer match reality.

$$\dot{\overline{x}} = \begin{bmatrix} \dot{\delta} \\ \ddot{\delta} \end{bmatrix} = \begin{bmatrix} 0 & 1 \\ 0 & 0 \end{bmatrix} \begin{bmatrix} \delta \\ \dot{\delta} \end{bmatrix} + \begin{bmatrix} 0 \\ K \end{bmatrix} v \tag{13}$$

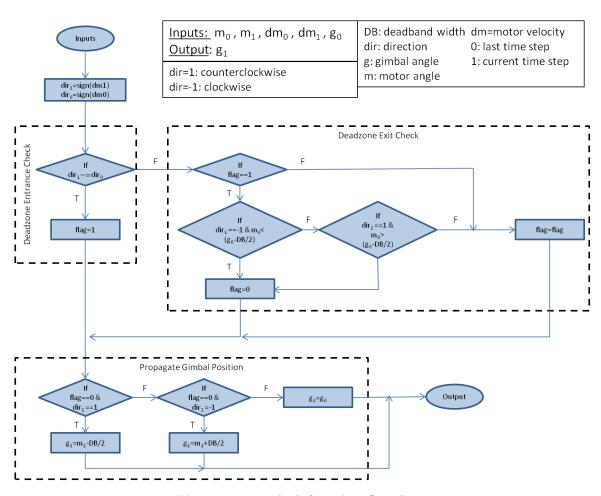


Figure 24. gearlash function flowchart

Incorporating Gear Lash Into the CMG Model.

As shown in Section 4.3, gear lash directly affects the performance of the CMG. To better investigate the effects of gear lash, it was incorporated into a CMG model. A function was created to simulate gear lash. This section presents how the gear lash

function is structured. The function is based on Simulink's Backlash block [22].

The gear lash function takes an input signal two points at a time, allowing for real-time implementation. The input signal consists of the angular position and velocity of the driving gear and the output is the angular position of the driven gear. Applied to the CMG, the driving gear is the motor (input), while the driven gear is the gimbal (output). The deadband width for the CMG is approximately 5°. Based on the input signal, the function operates in one of three modes:

Gears Engaged, Moving CCW The output angle is the equal to the input angle less half the deadband width.

Gears Engaged, Moving CW The output angle is the equal to the input angle plus half the deadband width.

Gears Not Engaged The output angle is equal to the previous value.

The gearlash function is illustrated in Figure 24. The gears become disengaged whenever the driving gear changes direction. The gears reengage when the difference between the input and output angles reaches half the deadband width. An example of the input-output relationship of the gear lash function is shown in Figure 26. In Figure 26a, note that the driven gear position holds its value (flat-lines) when the driving gear angle peaks.

One shortcoming of this method of modeling gear lash is that it does not take into account the physics of the reengagement of gears. The simulated output gear changes position by about half the deadband width over a single time step upon reengagement, resulting in an unrealistically high velocity for a single sample point, which can be seen in Figure 26b. This spurious data point can either be filtered out, or the physics of the reengagement can be modeled. However, this model of gear lash is accurate enough to replicate the time duration over which the gimbal angle does

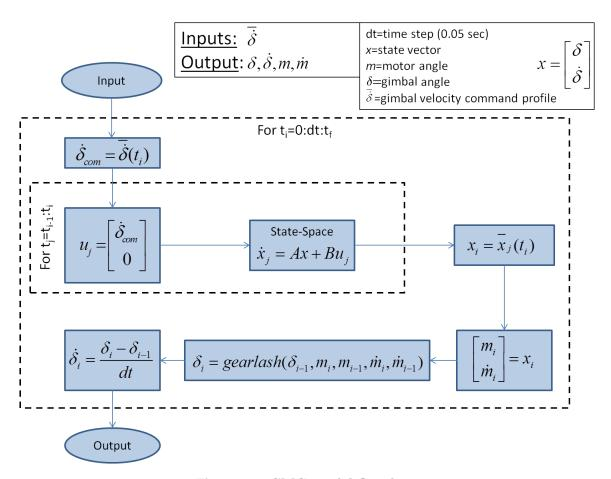


Figure 25. CMG model flowchart

not move, which is the primary purpose of the gear lash portion of the model. Gear lash is incorporated into the model by inputting the simulated motor angle calculated from the state space model into the gear lash function.

CMG Model Validation Test Procedures.

To validate the model, simulated results have to be compared to test results. As simulating gear lash is a major objective of designing the model, a sinusoidal command was chosen to test because it regularly changes directions. The gimbal was commanded with a sinusoidal wave of amplitude 0.5 rad/s, at a frequency of 0.2 Hz, for 30 seconds. Velocity, position, command, and input data were recorded during the test. The same input signal used for the test was input to the model using nominal

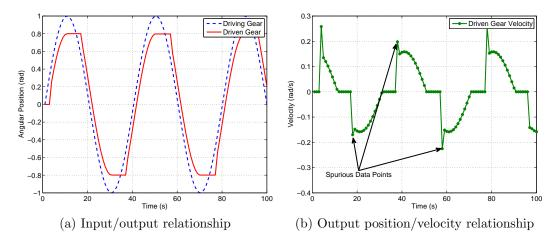


Figure 26. Example of gear lash function with a deadband width of 0.4 rad (23°)

values of 5° for the deadband width and 1 for the design variable K.

3.4.6 Simulated Maneuver.

Simulated Maneuver Test Introduction.

The CMG model validation test (Section 3.4.5) evaluates how well the CMG model matches the real CMG when commanded with a sinusoidal signal, which is not representative of operational commands. To gauge how well the CMG performs under operating conditions, the simulated maneuver test was performed. This test used a command signal representative of commands used in a real AFRL spacecraft simulator maneuver. This is the first test to incorporate the rotor of the CMG; all previous tests were conducted with rotor off. The objectives of the simulated maneuver test are to:

- Evaluate the performance of the real CMG given commands representative of operational use
- Evaluate how well the CMG model matches the real CMG under operational use

• Evaluate the performance of a PI controller on the real CMG under operational use

Simulate Maneuver Test Procedures.

The CMG MATLAB model was developed by Swenson and modified by this author in this presented research. A screenshot of the satellite animation the model produces is shown in Figure 27; the black triangle represents the spacecraft simulator, while the white box represents a generic payload. The simulation utilizes a four-CMG array. This simulation was used to determine an angular velocity profile to command the CMG. The simulated vehicle was commanded to perform a set of pointing maneuvers over a 90 second period, changing targets every ten seconds.

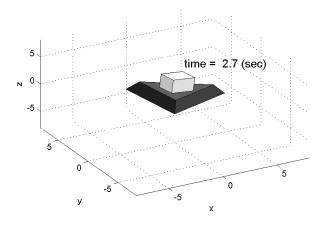


Figure 27. Animated representation of spacecraft simulator output by MATLAB model

The simulation outputs the command history of each CMG, the first of which is shown in Figure 28. The command history was saved for testing with the CMG. The command history signal is recorded before it is saturated by operating limits in the simulation. The real CMG was commanded with the simulation command signal while recording velocity and position data. The simulated maneuver test was then repeated for each of the four CMG signals, using the same physical CMG. Based on

test results performed as described in Section 3.4.4, which indicate that a PI controller may improve command tracking, a PI controller was incorporated into the real CMG with a proportional gain K_P of 1.1 and an integral gain K_I of 0.75. The simulated maneuver test was then repeated, for a total of eight times (four without PI control, four with PI control). The CMG rotor was spinning at 3500 rpm for all tests and the simulation. This rotor speed was chosen because the rotor is expected to operate between 3000 and 4000 rpm. The same command signal input to the real CMG was also input to the CMG model for further comparison. The design variables in the model were set to those calculated from the CMG model validation test (Section 4.7). Time delay was set to 0.8 seconds, K was 1.6918, and gear lash was 5.1638°.

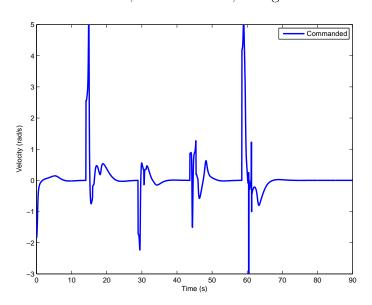


Figure 28. Command history for CMG # 1 from the spacecraft simulation

3.4.7 Vehicle-Level Model.

Vehicle-Level Model Test Introduction.

Until now, all tests have been concerned with the characteristics and performance of a single CMG. However, a main objective of this research is to understand how the array of CMGs impacts the performance of the AFRL spacecraft simulator. This section presents the methodology of a computational test performed to determine the effects of gear lash on overall vehicle performance. The spacecraft simulator model discussed in Section 3.4.6 does not have gear lash incorporated; gimbal angle and angular velocity always track perfectly with the commands. In reality, the gimbal lags the command signal and and is non-responsive to commands during direction changes due to gear lash. If gear lash is minimal, then it can be ignored within the model without significant disparities between simulation and reality. However, due to the CMG's large amount of gimbal gear lash, about 5°, this assumption cannot be made. The objectives of this test are to:

- Incorporate gear lash similar to that of the CMG into the overall vehicle model
- Determine the effects of gear lash on vehicle performance

Model Overview.

The spacecraft simulator model is written in MATLAB. The basic structure involves an outer loop for control and an inner loop for the dynamics, depicted in Figure 29. When the simulation initializes, a set of predetermined targets are assigned. As the outer loop iterates, the vehicle points itself to each target in turn. In the outer loop, angular error is calculated which determines a commanded angular momentum vector for the vehicle, which in turn determines the commanded gimbal angular rate required for each CMG. This gimbal rate is used to propagate the gimbal angle in the outer loop. The assigned gimbal angle is then assigned as a global variable to pass it between the inner and outer loops. The outer loop operates at the time step of the vehicle, and can be adjusted as an input. Nominally, a time step of 0.05 seconds (20 Hz) is used.

The inner loop simulates the physics of the vehicle using MATLAB's ode45 command. The inner loop iterates on a variable time step, determined by ode45, over

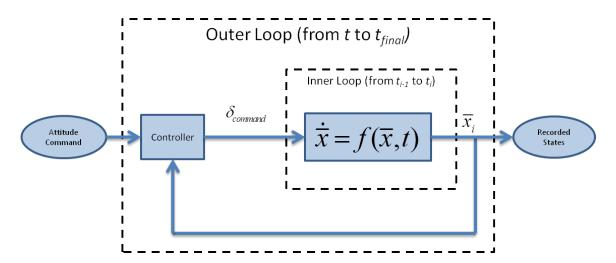


Figure 29. Block diagram of original spacecraft simulator model

the period of one outer loop time step (nominally 0.05 seconds). The outer loop time step is not the same as an inner loop time step, which varies according to the ode45 function. The state vector \bar{x} passed to the inner loop, shown in Eq. (14), contains the spacecraft quaternions \bar{q} , angular rates $\vec{\omega}$, and CMG gimbal angles $\bar{\delta}$. The inner loop iterates, solving for the state at the next time step until the end of the outer loop time step is reached. Even though the inner loop calculates the states at a finer resolution than the outer loop, only the last calculated value from the inner loop is stored, thus simulating the sampling frequency of the real system.

$$\overline{x}_{11\times 1} = \begin{bmatrix} \overline{q}_{4\times 1} \\ \overrightarrow{\omega}_{3\times 1} \\ \overline{\delta}_{4\times 1} \end{bmatrix}$$
 (14)

Incorporating Gear Lash Into Spacecraft Simulator Model.

The gearlash function used in Section 3.4.5 is also used in the vehicle-level simulation. Gear lash is treated as a pre-conditioner for the input state before passing into the inner loop, as shown in Figure 30. In Figure 30, m is the motor angle and \overline{x} is the state vector. The controller commands a gimbal angle, then the gearlash function,

which keeps track of the motor angle, determines whether or not the motor and gimbal gears are engaged. The *gearlash* function then overwrites the commanded gimbal angle with the actual gimbal angle. This updated state is passed into the inner loop, where the physics are simulated. The controller only "sees" the gimbal angle, not the motor angle, which is true of reality.

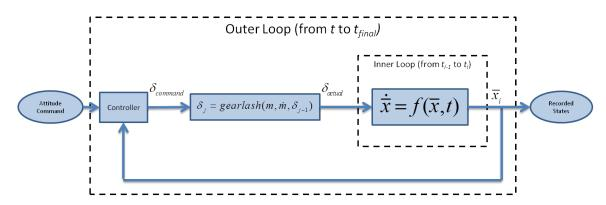


Figure 30. Block diagram of spacecraft simulator model with gear lash

Vehicle-Level Model Test Procedures.

For this computational test, the simulation was run given an arbitrary attitude command sequence over a 90 second period (the same parameters as the simulated maneuver test, Section 3.4.6). The simulation was run with three different levels of gear lash: 0°, 5°, and 10°. The zero configuration is a control test to compare a theoretical perfect gear train. The 5° test evaluates the nominal value for gear lash. The 10° test evaluates a worst-case scenario for gear lash. All tests were run with a 20 Hz controller, which is the sampling frequency of the real CMGs.

3.5 Summary

Chapter III presented the details of the CMG hardware and control software before describing the methodology and procedures of the tests utilized to characterize and evaluate the CMGs. Seven tests were described: sensor filtering, gimbal balance, sensor noise, PID control, CMG model validation, simulated maneuver, and vehicle-level model validation. Chapter IV presents the results and analysis of the tests described in Chapter III.

IV. Results

4.1 Introduction

This section presents the test results and analyses from all the tests discussed in Chapter III. The tests can be divided into two groups: hardware and modeling. The hardware tests (sensor filtering, gimbal balancing, sensor noise, and PID control) are presented first and are focused on characterizing the performance of the CMG. Next, the modeling tests (model validation, simulated maneuver, and vehicle-level model) concern creating and validating computer models of the CMG and the AFRL spacecraft simulator, which includes six CMGs.

4.2 Sensor Filtering Test

Sensor Filtering Test Results.

The first objective of the sensor filtering test is to characterize three filtering methods and one hardware method for determining the velocity of the gimbal, discussed in Section 3.4.1. The second test objective is to determine which of the tested filters to use on future tests. The three filters tested are a two-point derivative, a five-point derivative, and a Kalman filter, all of which calculate velocity from position encoder measurements. The two-point derivative filter serves as the control test; it takes the discrete derivative of two adjacent position measurements. The five-point derivative filter pre-conditions the input position to account for the angle roll-over condition that happens when the gimbal rotates from 359.9° to 0° (the resolution of the encoder is $\pm 0.1^{\circ}$), then calculates the discrete derivative of the two corrected position measurements. The filter then averages four velocity estimates (derived from five position measurements) and reports the average as the estimated velocity. The Kalman filter

takes the five-point derivative estimation as an input, then outputs a filtered estimate that takes the dynamics of the gimbal into account. All filtering methods are detailed in Section 3.4.1. The filters are compared against the Hall sensors, which output velocity directly.

The gimbal was run at a constant angular velocity while recording data from all filters. A segment of the results from the sensor noise filter test is shown in Figure 31. The position data is overlaid with velocity data to show position-induced anomalies. The negative spike at 35 seconds in the two-point filter data (blue solid line) is due to the angle roll-over condition. The other filters include a roll-over correction function, so those filters do not output the same spike in velocity. Because there is no method with which to externally measure the velocity of the gimbal, there is no "truth" data to compare against. Only the counter-clockwise test data is shown because the clockwise test data is nearly identical. The full-length test results are shown in Figure 32. For clarity, only the Kalman filter estimates are shown in Figure 32.

Sensor Filtering Test Analysis.

Figure 31 shows the results from the sensor filtering test described in Section 3.4.1. First, none of the measurements show the gimbal reaching the commanded velocity of 0.5 rad/s. This result is not unexpected, because the test does not incorporate a closed-loop feedback controller. Command tracking is not an objective of this test and is addressed in Section 4.5. Second, there is a disturbance torque applied to the system associated with the position of the gimbal which can be seen in the regularly spaced spikes in velocity estimates of the Kalman filtered data in Figure 32. This disturbance was later determined to be due to an imbalance in the system and is addressed in Section 4.3. Third, the measurements are stratified into two groups: the two-point filter and Hall sensor in one group, and the five-point and Kalman filters in the other

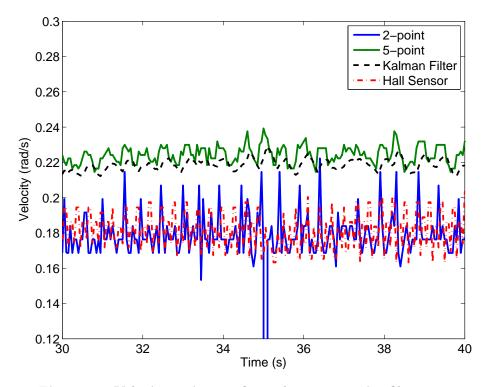


Figure 31. Velocity estimates from the sensor noise filter test

group. This stratification can be seen in Figure 31 by the velocity gap between the two groups. This grouping was likely caused by an error in the Simulink program that runs the CMG. Fourth, the five-point and Kalman filters produce qualitatively smoother data than the two-point and Hall sensor data. Quantitative analyses of the test data are presented here.

First, we address the groupings in the data likely caused by an error in the Simulink program. To test this hypothesis, the raw position data was post-processed through an identical five-point filter with roll-over correction. Figure 33 shows the post-processed five-point filter data with the "live" five-point filter data and the Hall sensor data (as an independent measure). The post-processed five-point data (derived in MATLAB script) is an improvement over the live five-point data (derived from Simulink), eliminating the velocity offset and placing the estimates more in line with the two-point and Hall sensor data. The exact source of the original five-point filter

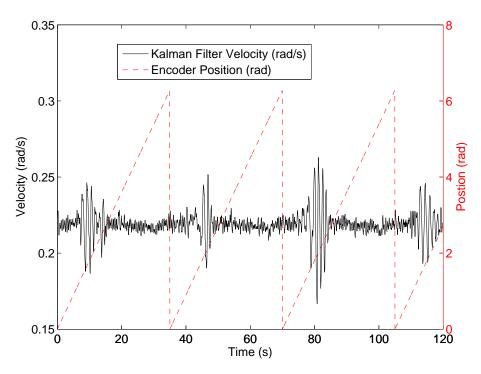


Figure 32. Full-length Kalman filter velocity estimates overlaid with encoder raw position measurements

error could not be determined, but if such a filter should be used in the future then the error should be diagnosed and fixed.

Because the Kalman filter estimates are based off of the live five-point filter and the Kalman filter is programmed within Simulink (it can only run with the CMG set up), a post-processing Kalman filter cannot be validated in the same way the post-processed five-point filter is. Therefore, the offset in Figure 31 is not removed for the Kalman filter data. A method is needed to validate the Simulink Kalman filter, but was not explored in this research. The "live" Kalman filter data can still be analyzed with regards to noise characteristics, but the actual values of the Kalman filter cannot be compared to other filters.

To examine another filter type that was not built into the Simulink model, a lowpass filter was applied to the two-point velocity data. A first-order filter was chosen with a cutoff frequency of 0.5 Hz [14]. The results of the lowpass filter are

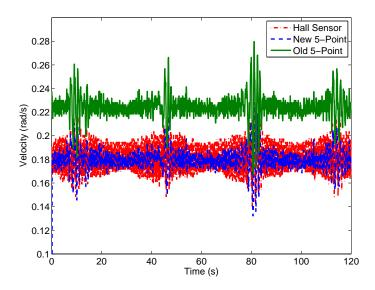


Figure 33. Old (live) and new (post-processed) five-point derivative filter

shown in Figure 34.

The root mean square (RMS) and standard deviation of each data set were calculated and are shown in Table 3. Ideally, the gimbal speed should have remained constant throughout the test. Therefore, higher variation in the data, indicated by RMS and standard deviation, can be attributed to sensor noise. The effectiveness of each filter can be measured by how well it rejects noise. By comparing the RMS and standard deviation between the filters, the two-point filter is shown to be the least effective because it has notably higher values for both metrics. However, standard deviation and RMS are more ambiguous in determining the *most* effective filter. For example, the Kalman filter has better (lower) standard deviation than the five-point filter, but the five-point filter has better RMS. To get better insight into the problem, the measurement distribution is analyzed.

Histograms of the measurement data are shown in Figure 35. The wide distributions in the two-point and hall sensor data, and more narrow distributions in the five-point, Kalman, and lowpass filter data are indicative of a smoother, better estimate of velocity. The Kalman filter velocity is offset along the x-axis in Figure 35

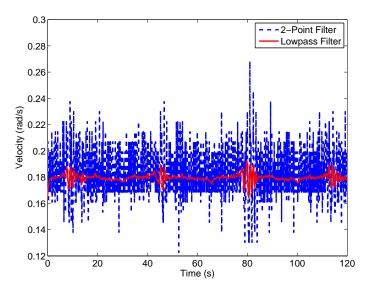


Figure 34. Lowpass filter with two-point derivative filter as input (1st order, cutoff frequency=0.5 Hz)

Table 3. Standard deviation and RMS of filter data

	CCW		CW			
Filter	STD	RMS	STD	RMS		
2-Point	5.125	5.124	5.127	5.126		
5-Point (Old)	0.010	0.225	0.012	0.225		
5-Point (New)	0.011	0.180	0.012	0.180		
Kalman	0.008	0.219	0.010	0.219		
Lowpass	0.003	0.180	0.003	0.180		
Hall Sensor	0.013	0.181	0.014	0.180		

because it was derived from the erroneously offset old five-point filter data.

The standard deviation of each filter is shown in Table 3. For each filter, the percentage of points within 1- σ was calculated. If the filters produce normally distributed data then 68.2% of the estimates would be within one standard deviation. Table 4 shows the percentage of data points within one standard deviation. Table 4 shows that 1) the five-point (both old and new), Kalman, and lowpass filters have similar distributions, 2) the two-point filter has a very narrow distribution, but this is due to its very large standard deviation (an order of magnitude more) compared to the other filters, and 3) the Hall sensor data has the highest σ of all the filtered

estimates.

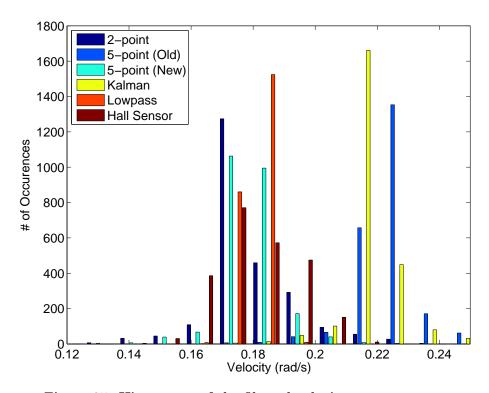


Figure 35. Histograms of the filtered velocity measurements

Table 4. Percent data points within 1- σ

Filter	CCW	CW
2-Point	99.8	99.8
5-Point(Old)	84.9	85.5
5-Point (New)	87.0	87.4
Kalman	84.9	85.0
Lowpass	82.4	84.8
Hall Sensor	60.1	72.3

Of the tested filters, using narrowness of data (percent within $1-\sigma$) as the chief metric, the five-point post-processed (new) filter is the most accurate. However, because the bug in the old five-point filter Simulink code was not discovered until after all tests in this thesis were completed, the Kalman filter was chosen as the velocity measurement source in all other tests. The average velocity of the Kalman and new

five-point filter data is 0.219 rad/s and 0.179 rad/s, respectively. The difference between the Kalman filter and new five-point filter average velocities is 0.040 rad/s. Because the difference in velocity is minimal, the effects of the slight error in filter choice likely have no effect on other tests conducted in this thesis.

The data from Tables 3 and 4 indicate that there is no significant difference between the clockwise and counter-clockwise tests. This suggests that there is no sensor bias associated with gimbal direction of rotation.

Sensor Filtering Test Conclusions.

Statistical analyses shows that the post-processed five-point filter estimations are the most reliable. This conclusion is based on the assumption that high variation in measurement data is due to sensor noise, and therefore an effective filter would have a minimum standard deviation and distribution of data points.

Improvement in the lowpass filter may be realized if further refinement in the cutoff frequency and transfer function order are investigated. Because the lowpass filter has similar σ values to the other filters, it may prove to be better than or useful if used in conjunction with the new five-point filter.

Due to a bug in the Simulink program that runs the CMG, an error in the fivepoint filter was not discovered until all tests were completed. Consequently, all tests were run using the Kalman filter estimated velocity, which was derived from the old five-point filter, as the measurement source. This error does not invalidate any tests because the difference between the Kalman filter and new five-point filters is minor.

4.3 Gimbal Balancing Test

Gimbal Balancing Test Results.

As previously discussed in Section 3.4.2, the rotor housing is not balanced about its axis of rotation, the gimbal axis, due to an electrical connector on one side of the housing. The effect of having an imbalance torque that depends on gimbal angle combines with gear lash to cause disturbance torques that cause uncontrollable accelerations of the gimbal. This gimbal balance test evaluates the effects of changing the total mass of a tunable mass balance on gimbal velocity measurements.

The gimbal was run at a constant angular velocity both with and without the tunable mass balance system installed. The first 100 seconds of angular velocity and position data from the CCW tests are shown in Figure 36. The unbalanced test is identifiable by the large spikes in velocity (Figure 36a), where gear lash developed. Note that both unbalanced and balanced data is shown in Figure 36b, but the distinction between the data is difficult to discern because the lines overlap very closely.

Gimbal Balancing Test Analysis.

The initial balancing of the rotor significantly reduces the gravity-induced disturbance torques; however, there is still an unbalance in the system, which can be seen as velocity spikes in the balanced data at 8, 47, and 76 seconds (Figure 36a). This remaining unbalance is due to the limits of the tunable mass balance, which uses approximately 5g washers and nuts as incremental masses.

Statistical analyses are used to interpret the data from the gimbal balance test. The distribution of data from each test, shown in Figure 37, indicates that, for both CW and CCW directions, the balanced rotor housing has less variance than the unbalanced housing. For both the balanced and unbalanced tests, the measurements are slightly biased toward the higher magnitude velocities which can be seen by the

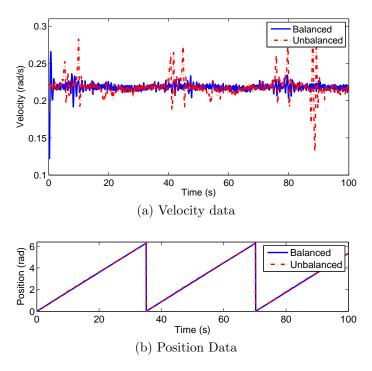


Figure 36. Velocity step response with and without tunable mass balance

skewing in Figure 37. This bias could be a result of sensor noise or a bias in the Kalman filter dynamics used to filter the measurements.

The standard deviations of the velocity measurements are shown in Table 5. The balanced tests show a decrease of 48% (CCW) and 35% (CW) in standard deviation.

Table 5. Standard deviation of gimbal balance test data

	CCW		CW	
	Balanced	Unbalanced	Balanced	Unbalanced
STD $(rad/s \times 10^3)$	5.84	11.94	4.55	13.00

Gimbal Balancing Test Conclusions.

Installing the mass balance is effective at decreasing the gravity-induced accelerations. Sudden uncommanded increases in velocity are caused by the combination of gear lash and mass imbalance. Balance along the gimbal axis can be improved upon, but will require a balance that either uses finer increments of mass than afforded by

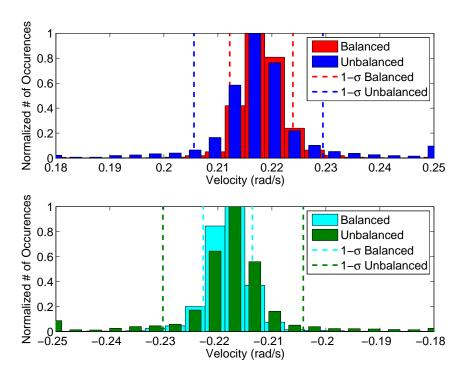


Figure 37. Gimbal balance test histogram (upper plot is CCW, lower plot is CW)

the five gram washers or allows for precise radial and axial adjustment of a static mass. Such a mass balance is already in development, and a concept design is shown in Figure 38. There is bias in the encoder measurements toward greater velocities. This bias could be caused by sensor noise or filter bias, but this test cannot determine the true cause. The bias is investigated in Section 4.4.

4.4 Sensor Noise Test

Sensor Noise Test Results.

Previous tests (Section 4.3) observed bias in the gimbal velocity measurements. The sensor noise test characterizes the encoder-derived velocity measurements (Section 3.4.3). Additionally, the sensor noise test determines if the gimbal operates linearly for steady-state velocity commands. Various angular velocities were commanded to the gimbal and the steady-state responses were recorded.

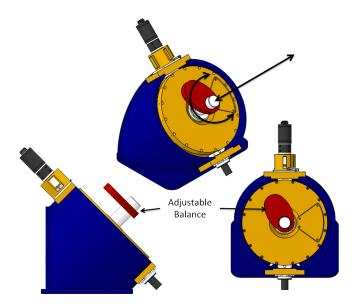


Figure 38. The adjustable gimbal balance concept design allows for radial and axial movement, as shown in the center graphic

The data from the sensor noise test are shown in Figure 39. The slowest velocities (around 0.1 rad/s on Figure 39) have frequent peaks. This was likely caused by stiction forces or torques. When the gimbal is moving around 0.1 rad/s, stiction forces dominate, and movement is noticeably jumpy, stopping frequently. Note that the measured velocities in Figure 39 do not correspond to the commanded velocities from Table 1. However, because the objectives of the sensor noise test are to characterize noise and linearity, the fact that the commanded velocities are not reached does not impact the analyses or conclusions. Command tracking is investigated in Section 4.5.

Sensor Noise Test Analysis.

This section presents analyses regarding Figure 39, which shows the results from the sensor noise test. Systematic errors are discussed, followed by statistical analyses of the results. Additionally, theories for statistical outliers are also presented. Because the commanded velocities are not met for all tests, the duration of this section will refer to the average *achieved* velocities of the test results, as opposed to the

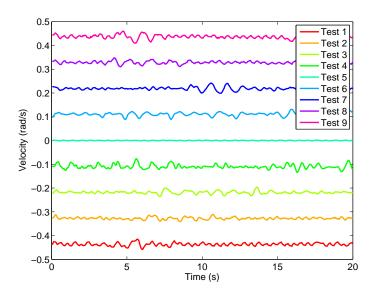


Figure 39. Sensor noise test data

commanded velocities. The mean of the actual velocities are shown in Table 6.

Statistical analyses are performed on all tests. The standard deviations, percent of data within 1σ (PW1 σ), and skewness are shown in Table 6. None of the tests have perfectly normal distributions of data. For all tests except the zero velocity, the distributions of data are more narrow than a normal distribution¹, which can be seen by the PW1 σ values in Table 6 (all are greater than 68.2%). Withstanding the outlier of zero velocity, the standard deviation varies by only 0.004 rad/s (0.25°/s) between the two most extreme values (-0.3 and -0.1 rad/s). Again withstanding the zero velocity outlier, all of the tests have a PW1 σ greater than 70%. This shows that the measurements vary by approximately the same magnitude with regard to velocity.

The relatively low PW1 σ value for the zero velocity data is caused by the low (an order of magnitude less) standard deviation. The zero velocity signal alternates between -0.0017 and 0.0016 rad/s, making it have the lowest variance of the tests. In reality, the gimbal is not moving at all during the zero velocity test.

 $^{^1\}mathrm{A}$ normal distribution has 68.27% of the data within one standard deviation

Table 6. Standard deviation (σ), percent within 1σ (PW1 σ), and skewness of sensor noise test data

Mean Velocity (rad/s)	$ \begin{array}{c} \sigma \\ (\times 10^3 \text{ rad/s}) \end{array} $	$PW1\sigma$	Skewness
-0.4	6.34	72	0.09
-0.3	4.87	74	0.30
-0.2	5.72	76	0.38
-0.1	9.15	73	0.73
0	0.90	59	-0.05
0.1	7.39	76	-0.82
0.2	6.42	79	0.13
0.3	5.77	72	0.09
0.4	7.76	77	-0.27

When the skewness² of the data is evaluated, it is shown that there is directionality to the measurement variation. Figure 40 shows the skewness of all test runs with the 1- σ bounds of all tests taken as a single data set. The ± 1 rad/s velocity points in Figure 40 are outliers caused by stiction forces inherent to the system. By examining the non-outliers, the values between the horizontal lines in Figure 40, an offset in skew can be seen between positive and negative average velocities. Negative velocities are skewed more to the right (positive skewness) than positive velocities. This direction-induced skew could be caused by uneven wearing on the gears, because the motor tested has many more hours running counter-clockwise (positive) than clockwise. It is tenuous to determine a source of bias based solely on the sensor noise test data. However, because the amount of skew was minimal, it would likely not impact the controllability of the system significantly.

The sensor noise test is the first test to observe different velocity responses in the gimbal. The same data can therefore be used to determine linearity in the system. The input-output relationship of the test data is shown in Figure 41 with 3- σ error bars around the data. First- and second-order polynomial fits are calculated for the average

²A skewness of 0 means that the distribution is perfectly symmetrical about the mean.

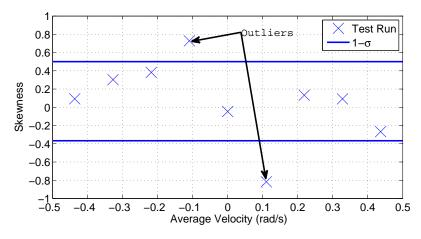


Figure 40. Skewness for sensor noise test

velocity versus commanded velocity relationship. The RMS errors for the first- and second-order fits are 3.275×10^{-4} rad/s and 3.0995×10^{-4} rad/s, respectively. Both fits resulted in RMS error less than the standard deviation of the velocities, therefore it is not possible to determine if the first or second-order fit is more accurate. Because the polynomial fits fit the data so well, the gimbal can be approximated as a linear first-order system. However, the first-order approximation does not apply over all operating conditions; it only applies for step inputs. Due to gear lash, discussed in Section 3.4.5, the system behaves nonlinearly during dynamic command tracking. Nonlinear behavior due to gear lash is detailed further in Section 4.7.

Sensor Noise Test Conclusions.

The first objective of the sensor noise test is to determine if the sensor noise behaves similarly over various operating velocities. The velocity measurements of the gimbal are statistically well-behaved, having minimal variation at all tested velocities. There is a slight skew to measurements, but not significant enough to impact controllability. Because the full range of -1 to +1 rad/s commanded velocities is not represented, the conclusions of this test can be only limitedly applied to velocities outside of the -0.5 to +0.5 rad/s range. Because the standard deviation of the data

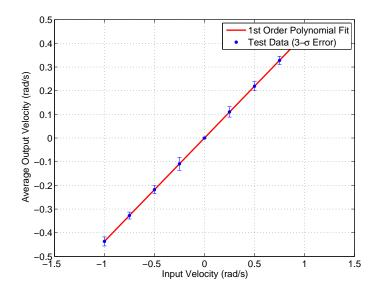


Figure 41. First-order polynomial fit to experimental data

did not vary significantly among the velocities tested, it is safe to assume the same of velocities outside of those tested. However, because of the direction preference of the skewness results, velocities outside of the -0.5 to +0.5 rad/s range should be investigated for a trend in skewness.

The second objective of the sensor noise test is to determine if the system behaves linearly for steady state velocity step commands. Under velocity step commands, the gimbal can be approximated as a linear first-order system. However, a wider range of velocities beyond ± 0.4 rad/s should be tested to confirm this approximation.

4.5 PID Control Test

PID Control Test Results.

The PID control test characterizes the behavior of the gimbal under different PID control gains. The gimbal was issued velocity step commands. Three sets of tests were run; each test varied either the proportional, integral, or derivative control gain while holding the other two constant.

The test data from the PID control test are shown in Figures 42 to 44. In Figure

42, note that the highest K_P value (1.5) causes near unstable behavior; this is why there are no further samples taken. Figure 44 indicates at what time the PD test was aborted to prevent damage to the gimbal motor due to high velocities.

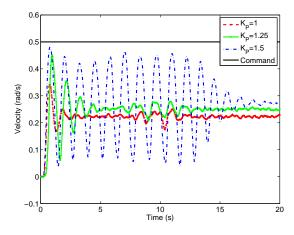


Figure 42. Step command test results from varying K_P ($K_I = 0, K_D = 0$)

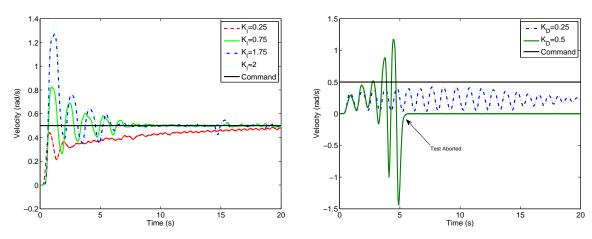


Figure 43. Step command test results from varying K_I ($K_P = 1, K_D = 0$)

Figure 44. Step command test results from varying K_D ($K_P = 1, K_I = 0$)

PID Control Test Analysis.

This section discusses Figures 42 through 44 which show the results from the PID control test. The only test that achieves better command tracking than open-loop is the K_I test (Figure 43). The system is very sensitive to changes in values of K_P and K_D because small changes in those control gains caused drastically different behavior

and, to a point, instability. Therefore, adjustments in K_I are the most effective method for fine tuning control of the gimbal.

Three common step response metrics, rise time, settling time, and percent overshoot, are calculated for the K_I tests, shown in Figure 45. With the exception of a K_I of 0.25, rise time is relatively constant throughout all values of K_I , so this metric does not weigh heavily into choosing an integral gain. There is a large change in the system dynamics between K_I values of 0.25 and 1, which can be seen in Figure 45 by the large decrease in settling time and increase in percent overshoot. It has not yet been determined what the requirements are for gimbal velocity overshoot or settling time; however, both of these metrics should be minimized. Some value of integral gain between 0.75 and 1 is a good starting range to investigate for control tuning. A more precise value can be determined with further testing and requirements definition.

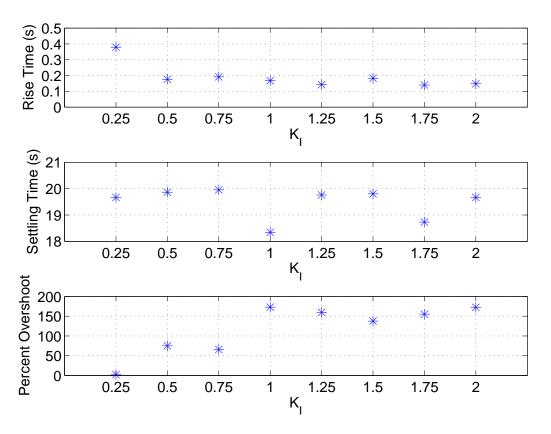


Figure 45. Step response metrics for variations in K_I ($K_P = 1, K_D = 0$)

The values tested for proportional gain K_P do not affect the system response with regards to command tracking. However, this does not rule out the use of a PI controller. If a PI controller is used, it will likely require a low (less than 1.25) K_P .

The values tested for derivative gain K_D affect the system response negatively, driving the system unstable with even low values. This instability is caused by the derivative term being proportional to the discrete derivative of the error [20]. Because the system is taking the discrete derivative between two points, measurement noise causes an artificially high signal to be fed into the derivative gain, causing the derivative control to dominate the proportional control. This difference in error can be seen in Figure 46 where the error derivative signal has much higher amplitudes than the error signal. One common solution to excessive derivative control is to apply a lowpass filter to the derivative input. However, adding such a filter will increase phase lag in the derivative control, counteracting the effectiveness of the K_D term, so a balance must be maintained.

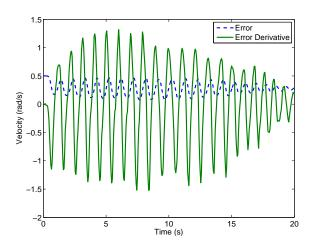


Figure 46. The error derivative term dominates over the proportional term, causing instability $(K_D = 0.25, K_P = 1, K_I = 0)$

PID Control Test Conclusions.

Integral control improved the gimbal's ability to track velocity step inputs. The system can operate stably under a wide range of K_I values, but the range between 0.75 and 1 exhibited the most optimal performance. Derivative control drives the system unbounded due to measurement noise. Further testing of derivative control incorporating a lowpass filter is recommended. It is also recommended to use caution when operating under derivative control, as the unstable velocities could damage the CMG. The system is mildly responsive to changes in proportional gain. Values of K_P greater than 1.25 cause instability in the system. Further testing of PI controllers should be performed with ranges of K_P between 1 and 1.25 and K_I between 0.75 and 1. Depending on the results of future filtered K_D testing, the addition of derivative control may further improve performance of a PI controller.

4.6 From Hardware to Models

Now that the CMG hardware has been characterized, the focus of this chapter now shifts to modeling. The first half of this chapter presents the analysis for how the CMG behaves; the second half presents how this behavior is modeled and how it affects the simulator test bed. Two models are presented: the CMG model (Sections 4.7 and 4.8) and the spacecraft simulator vehicle model (Section 4.9).

4.7 CMG Model Validation Test

4.7.1 CMG Model Validation Test Results.

A model of the CMG gimbal was created in MATLAB. The model, like the real CMG, has gear lash incorporated. To validate the model, a sinusoidal velocity command was input to the real CMG gimbal while recording velocity data. The same

command was input to the CMG model for comparison. The objectives of the model validation test are to create a model that incorporates gear lash and for said model to closely match real test data.

This section presents the results of the model validation test described in Section 3.4.5. A segment of the experimental results from the test are shown in Figure 47. The input signal is the commanded signal after it has been differenced with the measured signal. The sources of the signals for the CMG model validation test are shown in Figure 48. The input signal did not reach saturation limits³ during the test; the test input did not have any sharp discontinuities due to saturation.

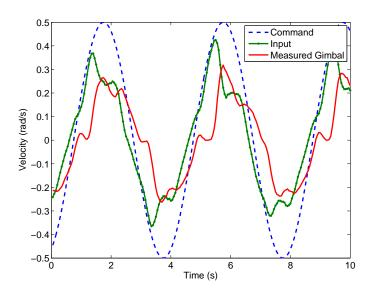


Figure 47. Gimbal velocity sinusoid command test results

A segment of the simulated results from the gimbal model using the input signal from Figure 47 as the model input are shown in Figure 49. The signal labeled "model motor" is the model output without gear lash (driving gear); the signal labeled "model gimbal" is the model output with gear lash (driven gear). Note the flat segments in the gimbal signal between 1.5-4 and 5.5-8 seconds; these segments indicate that the simulated gears were disengaged. The sharp spikes in the velocity plot in Figure 49

 $^{^3 \}text{Gimbal saturation limits: Acceleration} < 5 \text{ rad/s}^2, \text{Velocity} < 100^\circ/\text{s} \; (1.745 \text{ rad/s})$

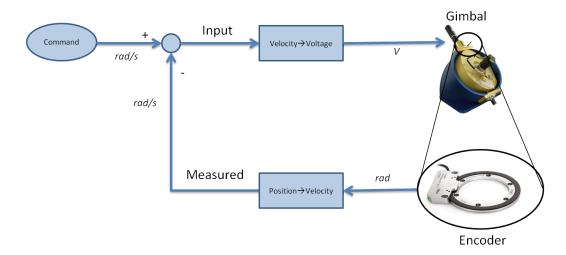


Figure 48. Diagram of signal sources for CMG model validation test [1]

are due to unrealistic accelerations discussed in Section 3.4.5.

4.7.2 Initial Analysis.

The large differences in velocity in Figure 49 indicate that the design variable K was not set correctly. This result was to be expected, because there was no previous indication of what value K should be, so the arbitrary value of 1 was chosen. In order to determine a more optimal value for K the simulation was executed multiple times with different K values. To measure the effectiveness of the K values, the RMS error between the truth data and model data is used as a metric. The cost function for varying K is

$$Cost = RMS_{error,position} + RMS_{error,velocity}. (15)$$

The results of tuning K are shown in Figure 50. The minimal cost is with a K of two. This value is chosen as a starting point for further tuning.

The velocity plot in Figure 49 also shows that the model is time shifted from the truth data. An initial guess value for this time shift can be calculated by examining

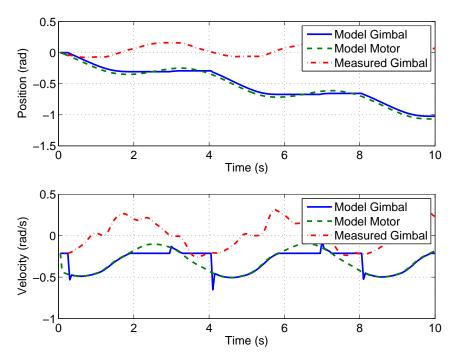


Figure 49. Experimental and modeled gimbal results given identical input signal

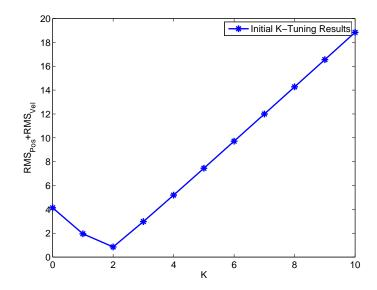


Figure 50. Optimizing RMS error by varying K

the peak-to-peak time of the velocity plot. Because the simulated gimbal is disengaged during much of the peak duration, the peak-to-peak time of the motor angle is used to determine an initial guess for the time shift value, as shown in Figure 51, which is a zoomed view of Figure 49. Using this method, the time shift is determined to be 0.8 sec.

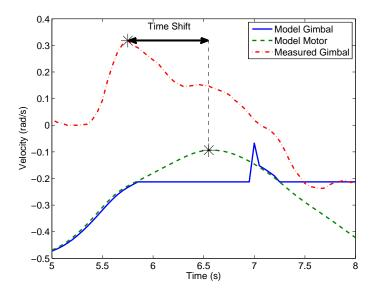


Figure 51. Peak-to-peak time determining initial guess for time shift

It is not possible to determine how accurate the initial guess of 5° gear lash is using only the data in Figure 49. The poor K chosen for the initial model test caused the simulated gimbal to be disengaged much of the time, leading to unrealistic behavior in gimbal position. A more accurate gear slack value can be determined only after a new K is chosen.

4.7.3 Model Tuning.

To make the model more accurate, MATLAB's fmincon function was used to optimize the system design variables. Fmincon uses constrained nonlinear optimization to find the local minimum of a function [23]. The cost function used was the same as used for choosing K (Eq. (15)). The system has three design variables: K, time

shift, and gear slack. All three variables are optimized at once using fmincon. The bounds and initial conditions input to the minimizing function are shown in Table 7. The bounds for K are based on the analysis from Figure 50. The bounds for time shift allow the optimizer to shift the signal over one period of the sinusoid signal forward in time. The bounds for gear lash are set relatively wide because the gear lash function does not perfectly replicate the physical gear lash and wide bounds allows the optimizer to compensate for the unrealistic dynamics.

Table 7. Minimizing function bounds and initial conditions

Design Variable	Lower Bound	Upper Bound	Initial Condition
K	1	3	2
Time Shift (s)	0.1	6	0.8
Gear Lash (°)	0	7	5

The minimizing function results are shown in Table 8. The initial guesses for gear lash and time shift are close to the tuned values, which makes the result for the abstract K value more convincing than if all the tuned design variables were drastically different from their initial conditions.

Table 8. Model tuning results

Design Variable	Before Tuning	After Tuning
\overline{K}	1	1.6918
Time Shift (s)	0	0.8
Gear Lash (°)	5	5.1638
Cost	1.9507	0.1825

The model was re-run with the tuned design variables; the results are shown in Figure 52. The simulated gimbal more closely tracks the real gimbal in both position and velocity. The duration of the simulated gear lash closely matches the duration of the real gear lash; this can be seen on the velocity plot of Figure 52 by comparing the relatively flat areas of the truth signal to the flat areas of the modeled gimbal signal.

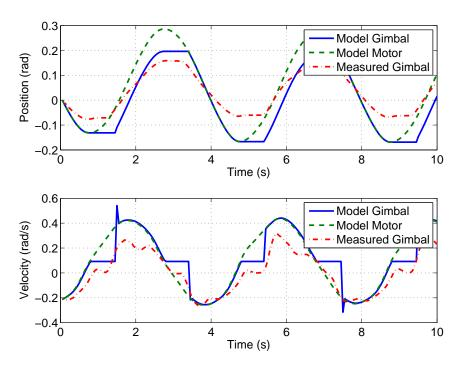


Figure 52. Model versus experimental results with tuned design variables

However, the model is not a perfect match to the test data.

The model differs from the test in two major areas. First, the model shows the gimbal moving across a greater band of both velocities and amplitudes. This is most apparent in the position plot of Figure 52, where the truth data is entirely within the bounds of the modeled gimbal data. This disparity in amplitudes can also be seen in the standard deviation of the data, shown in Table 9, where the model has higher standard deviations in both position and velocity than the real data. The real gimbal is not able to track the command signal as well as the modeled gimbal.

Table 9. Standard deviation of model versus real test data

	Standard Deviation			
	Model Truth			
Position (rad)	0.14	0.08		
Velocity (rad/s)	0.22	0.17		

Second, the real gimbal exhibits deviations in the velocity data, occurring near

peaks in velocity, which the model does not replicate. Because these deviations do not occur in the motor signal either, and the only difference between the model's motor and gimbal data is the use of the gear lash function, the truth velocity deviations are caused by dynamics that were not captured in the model. The deviations are caused by gear float, where the decrease in velocity of the motor caused the gears to disengage, allowing the gimbal to continue on with its current velocity. The error caused by this gear float is eventually counteracted by the feedback control. This mechanism is illustrated in Figure 53, where the gears become disengaged at point A, and the gears reengage at point B. Modeling such dynamics is possible; however, control laws such as PID control discussed in Section 3.4.4 may compensate for floating gears without a need to create a more complex model. The deviations may also be caused by non-constant friction in the gimbal assembly, which can also be modeled.

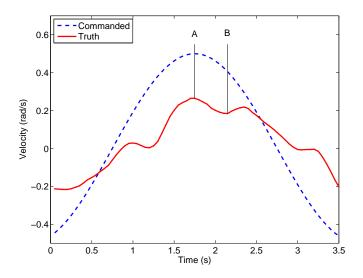


Figure 53. Gears disengage at A, then reengage at B

4.7.4 CMG Model Validation Test Conclusions.

The first objective of the CMG model validation test is to create a model that simulates gear lash. This objective was completed, although the modeled gimbal angle

matches measured data only in the duration of time that gears spent disengaged. The model does not accurately predict velocity amplitudes during gear lash. Amplitude modeling can be improved through modeling gear-on-gear interactions, although such a high-fidelity model may not be necessary to predict CMG performance.

The second objective of the CMG model validation test is to create a model of the gimbal that closely matches test data. The CMG gimbal model performed reasonably well, although further testing and analysis is required before the utility of it can be determined. The model may be robust enough for rough order of magnitude simulations, but it is not accurate enough to be incorporated into any feedback control. The primary difference between the model and reality is gear floating caused by gear lash. The addition of controls may serve to lessen the severity or eliminate the gear floating issue. If gear float can be minimized, the model may match experimental data better. If the model does not match controlled gimbal data, then the dynamics of the model will have to be updated, taking into account independent dynamics of the gimbal gears and/or friction. The CMG model validation test is repeated in Section 4.8 using a simulated maneuver, which is a more accurate representation of operational commands than a sinusoidal input.

4.8 Simulated Maneuver Test

4.8.1 Simulated Maneuver Test Results.

The simulated maneuver test used a gimbal angle command history from the spacecraft simulator model as an input to the real CMG, as shown in Section 3.4.6 (Figure 28). The first objective of the simulated maneuver test is to evaluate the performance of the CMG under operating conditions. The other two objectives of the simulated maneuver test are to evaluate a PI controller and evaluate the CMG model from Section 4.7. Based on data from Section 4.5, a PI controller was also

tested with the simulated command history. Because the spacecraft simulator model utilizes four CMGs the test was repeated, commanding the real CMG with each of the simulated command histories. A total of eight tests were run: one for each CMG (four) with and without PI control. The same commands were also input to the CMG model for comparison.

The results from the simulated maneuver test are shown in Figures 54 and 55. Results from all simulated CMG signals are similar; only results from CMG #1 are shown for clarity. In Figure 54, note the instability in the PI-controlled signal. The uncontrolled signal in Figure 54 and the measured signal in Figure 55 are the same.

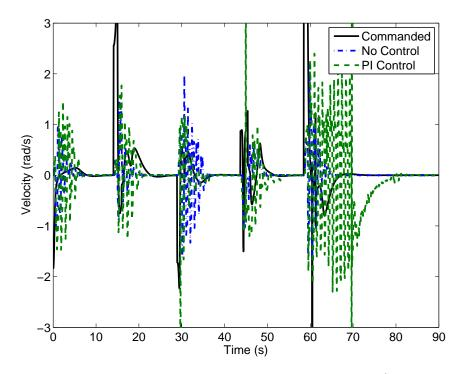


Figure 54. Uncontrolled versus PI control results for CMG # 1 ($K_P = 1.1, K_I = 0.75$)

4.8.2 Simulated Maneuver Test Analysis.

This section presents the results of Section 3.4.6, the simulated maneuver test, the results of which are shown in Figures 54 and 55. The open-loop CMG angular rates tracked the command signal with a RMS error of 1.29 rad/s, which is relatively

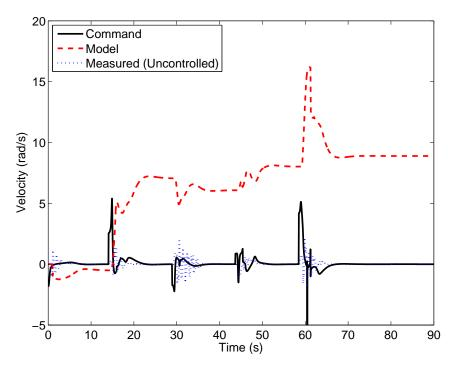


Figure 55. Uncontrolled versus modeled results for CMG # 1

small.

The PI controlled test caused excessively slewing in the gimbal, as can be seen in Figure 54 by the large spikes in the PI data. The RMS error of the PI controlled test is 6.04 rad/s, whereas the RMS error for the uncontrolled test is 1.29 rad/s. Because the uncontrolled test has less error than the controlled test and the only major difference between the two tests is the addition of integrator control, the inputs from the controller are examined. Figure 56 shows the component input signals from the controller for CMG #1.

The K_P signal in Figure 56 is the error multiplied by the proportional gain (1.1). The K_I signal in Figure 56 is the integrated error multiplied by the integral gain (0.75). The proportional signal has generally more erratic and larger inputs. However, the proportional term always returns to a value close to zero. Conversely, the integrator term has smoother trends, but acquires a bias throughout the test. The median values for the proportional and integral control signals are shown in Table 10.

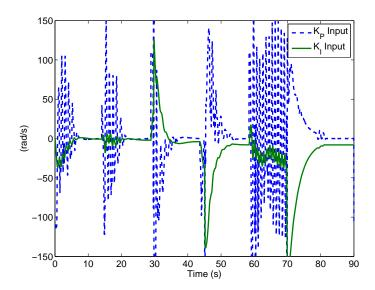


Figure 56. Individual components of controller inputs for CMG # 1

Table 10. Median of individual controller component terms for all CMGs

Controller Term	CMG #1	CMG #2	CMG #3	CMG #4
Median K_P Input (rad/s)	0.00	-0.01	-0.30	-0.37
Median K_I Input (rad/s)	-14.27	-17.45	-18.78	-20.65

The median errors in Table 10 show that the integrator term of the PI controller was constantly driving the velocity of the gimbal. This mechanism is known as integrator windup and is caused by the integrator term constantly building from previous errors [20]. The controller tested does not include any integrator windup protection measures, which would have prevented the oscillations. There are various methods to prevent integrator windup, including saturating the output of the integrator, regularly resetting, or using a fading memory filter on the input of the integrator term. Integrator windup likely did not appear in the PID test (Section 4.5) because the tests were not run for long enough for windup to become a significant effect.

The modeled gimbal velocity results did not match well the command signal or the test results. The RMS error of the model velocity was 8.98 rad/s. However, the RMS error as a metric does not apply well to the model data, as the model calculated a nearly static offset of about 10 rad/s, starting at about 20 seconds (Figure 55). This poor match was also caused by dissimilar test procedures, this time with the model validation test (Section 4.7). The model validation test was performed with the rotor off. Consequently, there were no gyroscopic forces acting on the gimbal motor during that test. Gyroscopic forces resist rotation on the gimbal axis, emulating friction. Therefore, when the design variables were tuned in Section 4.7, they were tuned for a "frictionless" (or at least less friction) gimbal. The effect of this can be seen in Figure 57, which is a zoomed in frame of Figure 55. At 14 seconds test time, the command signal input a 5.4 rad/s slew. The real gimbal responded at first with a slight irregular increase in velocity, then decrease, then rose to a peak of 1.43 rad/s at 15.45 seconds. The model responded with a rise to 5.1 rad/s. In Section 4.7, the model exhibited behavior of not matching reality well around zero velocity, so the fact that the model did not replicate the irregular deviations at the onset of the command was not unexpected. However, that the model did not match the final rise to 1.43 rad/s is indicative of poorly-tuned design variables. To make the model match reality, either the model validation test should be performed again using a spinning rotor, or the model dynamics should have the rotor speed incorporated into them.

4.8.3 Simulated Maneuver Test Conclusions.

The simulated maneuver test determined that the CMG tracks velocity commands with minimal error. The tested PI control gains degrade performance of the gimbal as compared to an open-loop condition due to integrator windup. Integrator windup can be remedied with a variety of solutions; one or more should be incorporated before using the CMG in a "real" test on the spacecraft simulator. The gimbal model did not replicate reality well because the model was tuned without the rotor running. The gimbal model can be made more accurate by retesting with the rotor running or

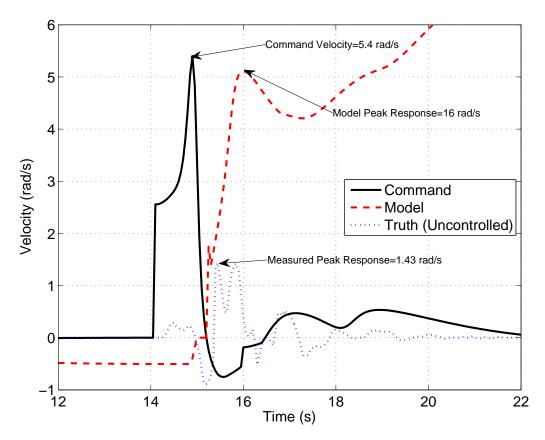


Figure 57. CMG model responds to command amplitudes more accurately than real CMG

incorporating rotor speed into the dynamical model.

4.9 Vehicle-Level Model Test

4.9.1 Vehicle-Level Model Test Results.

This section presents the results from the vehicle-level model test (Section 3.4.7). The vehicle-level model test objectives are to incorporate gear lash into the overall spacecraft simulator model and determine the effects of gear lash on spacecraft simulator performance. This was a computational test; no hardware was involved. The spacecraft simulator model was modified to include gear lash. The simulation was run three times, with different amounts of gear lash (0°, 5°, and 10°).

Figures 58 to 60 show the simulated gimbal angle and motor angle as a function

of time. For clarity, only CMG #1 test data is shown throughout this section. All other CMG data show common behaviors. The black boxes at the bottom of Figures 58 through 60 indicate times during which gear lash is active, when the motor gear was not engaged with the gimbal gear. In the 0° gear lash case (Figure 58) the gears did not disengage at all, so the black boxes are only indications of motor direction change, not gear disengagement. All data was taken with a sampling frequency of 20 Hz.

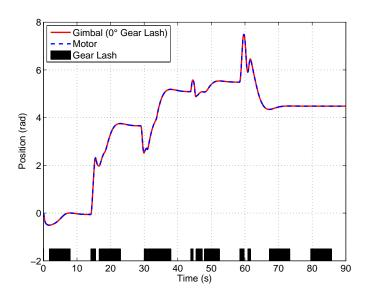


Figure 58. Simulated gimbal and motor angles with 0° gear lash

Figure 61 shows a zoomed in view of a the gimbal and motor data with all three tests overlaid on the same plot. The gimbal and motor angle for the 0° case cannot be differentiated from each other because the data represented an ideal gear train.

The angular momentum data from the vehicle-level model test are shown in Figure 62. Each plot in Figure 62 shows the individual components of the angular momentum in the inertial frame. The CMG angular momentum data in Figure 62a is the angular momentum of the entire CMG array (all six CMGs). The total angular momentum plot in Figure 62c was calculated by adding the CMG and spacecraft angular momentum vectors. The times over which the spacecraft simulator was changing

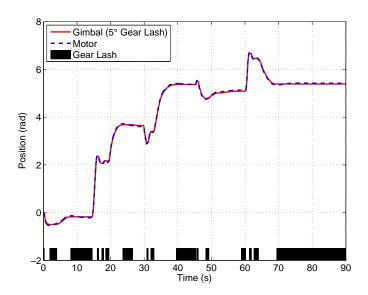


Figure 59. Simulated gimbal and motor angles with 5° gear lash

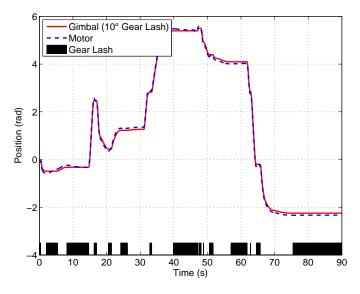


Figure 60. Simulated gimbal and motor angles with 10° gear lash

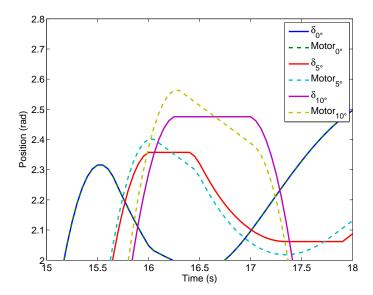


Figure 61. Zoomed in simulated gimbal and motor angle data for all tests

commanded targets is seen by the large spikes in data (a total of five spikes, one for each maneuver). A maneuver begins when the spacecraft starts rotating, when the angular momentum changes. The portions of the plots where the component angular momentum values dwell near zero indicate that the commanded attitude was reached and no torque was being commanded.

4.9.2 Vehicle-Level Model Test Analysis.

The first objective of the vehicle-level model test is to incorporate gear lash similar to that of the real CMG into the overall spacecraft model. Before proving if this objective is accomplished, a common-sense check on the model's validity is first performed. Because there are no external torques modeled in the simulation, the total angular momentum of the vehicle (spacecraft body and CMG array) in theory must remain constant. This conservation of angular momentum condition is not met, as can be seen in Figure 62.

The test was performed with a spacecraft initial angular velocity equal to zero and initial gimbal rates equal to zero. Therefore, the initial angular momentum of

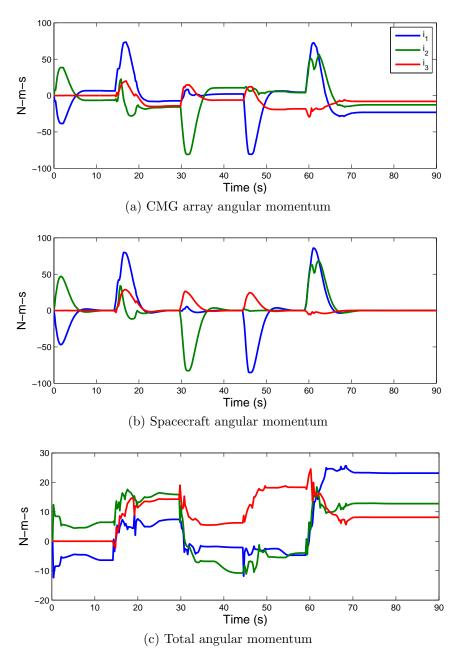


Figure 62. Angular momentum from new spacecraft model simulation (5° gear lash, 20 Hz sample frequency)

the total vehicle was zero. If the model is perfectly reflective of reality, all components in the total angular momentum plot of Figure 62 should sum to zero at every time step. However, the flat sections at the end of the data sum to non a non-zero value. The simulation started with a total angular momentum (the magnitude of the three components in Figure 62c) of zero. The simulation ended with a total angular momentum of 18.3 N-m-s.

The violation of conservation of angular momentum is likely a computational error caused by changing states, namely gimbal angles, outside of ode45 (the inner loop of the simulation). Any parameters that change within the inner loop are solved for at very fine time steps (80 Hz when the simulation is operating at 20 Hz). Consequently, errors do not build up very significantly within the inner loop; any error build-up in the state vector is not detectable. However, the spacecraft simulator model changes gimbal angle in the outer loop when the controller assigns new gimbal angles. Because the outer loop does not take any physics into account when assigning gimbal angles, unlike the inner loop, more significant error build-up occurs.

To test this hypothesis, the simulation was run again under different controller sample frequencies. If the hypothesis that the outer loop is not incorporating real physics causes error build up is true, then the angular momentum should respond to changes in controller sample frequency. A higher sampling frequency would decrease angular momentum error and a lower sample frequency would increase angular momentum error. If the hypothesis is not true, and the simulated angular momentum does not respond to changes in sample frequency, then the error is caused by an unknown source. The simulation was run with sample frequencies of 5 Hz and 300 Hz, both with a gear lash of 5°; the results are shown in Figure 63 along with the nominal test results at 20 Hz.

Figure 63 shows that the total angular momentum of the vehicle changes more

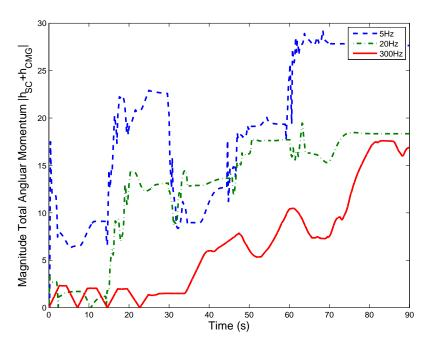


Figure 63. Controller sampling frequency effects on angular momentum (5° gear lash)

with decreased sample frequency. This results proves the hypothesis that the error of model not conserving angular momentum is caused by changing gimbal angles in the outer loop of the simulation. To determine if the error was caused specifically by the implementation of gear lash into the model, the original spacecraft simulator model (Figure 29) was run through the same maneuver simulation with a sample frequency of 20 Hz; the results are shown in Figure 64.

Figure 64 shows that the angular momentum changes throughout the old model. This result was expected because the old model assigned gimbal angles in the outer loop. The changes in angular momentum from the old model and the new model are shown in Table 11. The new model builds up a higher error in angular momentum than the old model (18 as opposed to 9 N-m-s) because the new model incorporates gear lash; the controller issues higher magnitude commands to compensate for the gear lash, which results in greater "non-physical" slews in the outer loop.

Because both the old and new models do not maintain constant angular momentum, the error is systematic to the model, it is not caused by incorporating gear lash

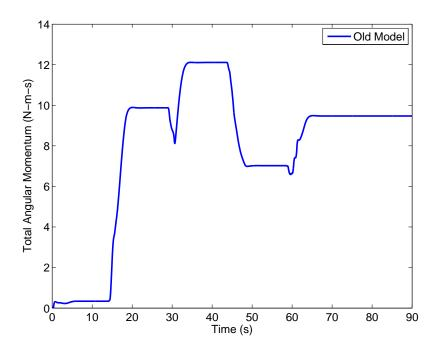


Figure 64. Old spacecraft simulator model angular momentum results with same maneuver commands as new model test (no gear lash, 20 Hz sample frequency)

Table 11. Changes in total angular momentum from beginning to end of simulations (no gear lash in old model, 5° gear lash in new model)

	Old Model	New Model		del
	20 Hz	5 Hz	20 Hz	300 Hz
Initial Angular Momentum (N-m-s)	0	0	0	0
Final Angular Momentum (N-m-s)	9.47	27.64	18.35	16.91

into the model. The angular momentum error is caused by a combination of factors: state changes in the outer loop, integrator time steps, and singularies. If all gimbal angle changes in the outer loop are moved to the inner loop, the conservation error would be lessened because the state changes would happen over a lesser time step. The error may also be caused by time step settings in ode45, which used a variable time step. Using a fixed step integrator, a higher order integrator, or an integrator with a constraint on angular momentum will improve the angular momentum error. Total angular momentum in Figure 63 changes when the gimbal velocities are commanded to extremely high velocities. Gimbal velocities increase rapidly because the

CMG array is approaching a singularity condition. If singularity avoidance measures were incorporated into the model, the singularity events would not occur and the high gimbal velocities would not be commanded. Preliminary simulations were run using singular value decomposition and showed improvement in the angular momentum error. Because the angular momentum condition is not met in the new model, the results cannot be used to predict behavior of the real spacecraft simulator system. However, the model can still be used to compare effects of different values of gear lash, which is the second objective of the vehicle-level model test.

The primary purpose of the ACS is to point the spacecraft at a target. Therefore, pointing error was chosen as a metric to compare the spacecraft simulator model with different gear lash amounts. The angular error from boresight of the spacecraft simulator to the target attitude was calculated for each simulation (all simulations on new model), shown in Figure 65. Two primary observations are made from Figure 65:

1) the vehicle always reaches the target attitude regardless of gear lash and 2) gear lash causes a delay in reaching the target attitude. The first observation is identified in Figure 65 by the flat lines at 0° error for every maneuver. The second observation is identified by the progressive delay in response times for increasing gear lash. The 0° lash test is the control for this test.

The response times for each maneuver are shown in Table 12. The times at arrival for each maneuver are shown in Table 13. A maneuver is defined as complete when the error reached less than 0.1°. The simulation requires that the spacecraft simulator remain on-target for ten seconds before progressing to the next target. Because the gear lash causes a delay in reaching the commanded target attitude, the delay builds up throughout the whole maneuver. While a delay from one attitude to another is less than one second for the 5° case (Table 12), the whole maneuver takes 1.65 seconds longer than the control case (Table 13). For the 10° case, the

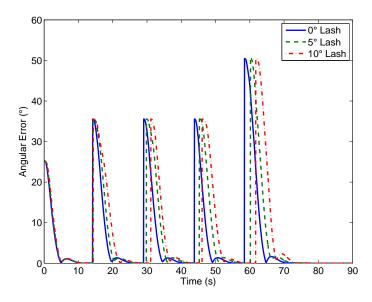


Figure 65. Pointing error for all tests

whole maneuver takes 3.2 seconds longer than the control case. Although gear lash does not have a significant effect on the response times of individual maneuvers (and in some cases actually improves response time), the delay is cumulative over series of maneuvers. The amount of delay increases with gear lash and the number of maneuvers in a sequence. Individual maneuver response time is delayed more for larger gear lash, but the 10° case tested represents a gear train with severe wear or of poor manufacturing quality. With average gear lash, 5° or less, the time delay for individual maneuvers is minimal.

Table 12. Time to complete each maneuver (maneuver complete when error $< 0.1^{\circ}$)

	Time to Complete Maneuver (s)				
Gear Lash	Maneuver #				
	1	2	3	4	5
<u>0</u> °	4.90	20.25	14.85	14.55	15.75
5°	5.00	20.95	15.45	14.95	15.60
10°	5.05	22.20	14.95	15.65	15.65

Table 13. Overall simulation time when maneuver was completed (maneuver complete when error $< 0.1^{\circ}$)

	Time at Arrival (s)				
Gear Lash	Maneuver #				
	1	2	3	4	5
	4.90	25.15	40.00	54.55	70.30
5°	5.00	25.95	41.40	56.35	71.95
10°	5.05	27.25	42.20	57.85	73.50

4.9.3 Vehicle-Level Model Test Conclusions.

The objectives of the vehicle-level model test are to incorporate gear lash into the overall vehicle model and determine the effect of such gear lash on vehicle performance. Incorporating gear lash into the model was achieved, but it was determined that the spacecraft simulator model does not maintain conservation of angular momentum. This condition must be met if results from the model are to be applied to real hardware. The model does not maintain total angular momentum. Both the old (without gear lash) and new (with gear lash) models modify states in the outer loop. The error is caused by a combination of state changes in the outer loop, the time step size used in the integrator, and singularity events. Although the model, in its current state, cannot be compared with real hardware, it can still be used to compare effects of different values of gear lash.

Gear lash does not have a significant effect on individual maneuver times for the spacecraft simulation. However, gear lash causes a more pronounced delay when acting over a sequence of vehicle maneuvers. Gear lash needs to be taken in to account when simulating the vehicle over sequences of commands. The effects of gear lash on vehicle performance were analyzed in qualitative terms; however, due to the incongruity in the model's angular momentum, gear lash effects on the vehicle could not be evaluated quantitatively.

4.10 Summary

Chapter IV presented the results and analyses of the tests used to characterize and evaluate the CMG. The tests were divided into two categories: hardware characterization and models. Qualitative conclusions about the various tests were made after data were analyzed quantitatively. Chapter V presents the overall thesis conclusions and recommendations for further work based on the results in Chapter IV.

V. Conclusion

5.1 Introduction

This chapter presents the concluding remarks and recommendations for future work for this research. Each section is divided into two corresponding subsections: hardware and models, which reflect the main areas of emphasis for this thesis. The hardware sections concern the the physical hardware and controls that run the CMG. The model sections concern the two models utilized in this research: the CMG model and the spacecraft simulator model.

5.2 Conclusions

5.2.1 Hardware.

All tests in this research focused on the performance of the gimbal. The magnetic position encoder is the primary telemetry source for the gimbal angle; the Hall sensor in the motor was concluded to be not as accurate as the encoder. The raw measurements from the position encoder are noisy, but were improved by passing the measurements through a Kalman filter, as seen in Section 4.2. The Kalman filter requires further refinement in its dynamics, but in its current state eliminates much of the encoder noise. Further improvements can be realized by incorporating a lowpass filter into the encoder measurements.

The tuneable mass balance added to the gimbal in Sections 3.4.2 and 4.3 decreased the magnitude of disturbance torques caused by imbalance. The presence of gear lash makes the existence of gravitational disturbance torques quite noticeable in the gimbal angular position measurements. Gear lash exaggerates the disturbance torques, but the mass balance minimizes the torques. Gear lash is a pervasive mechanism in the

gimbal performance that should not be neglected when testing. The tuneable mass balance can be improved on and an new version is in development.

The measurements from the position encoder are statistically predictable, as shown in Section 4.4. The gimbal behaves as a linear system when tracking velocity step inputs. However, it was shown that the linear behavior applies only in a limited operating range. The full operating range of the gimbal velocity was not tested. Furthermore, linearity applies only with step commands, not moving commands.

The performance of different PID controllers on gimbal velocity was tested in Section 4.5. Integral control improves command tracking; the gimbal cannot reach a commanded velocity without integral control. Proportional control does not affect the gimbal performance significantly, but may be used for minor tuning. Derivative control, in its current state, causes the system to become unstable. Instability is caused by the derivative control term using the discrete time derivative without any filtering, which results in a very noisy signal that dominates the control signal. Derivative control can be improved using a lowpass or moving average filter. Integrator windup causes excessive oscillations in the gimbal; a form of windup protection can and should be easily implemented into the controller for future tests.

5.2.2 Models.

An analytical model of the CMG gimbal was created in MATLAB (Section 4.7). The model closely predicts the nonlinear dynamic behavior of the real CMG with 5° of gear lash. This model was tuned to match test data of the gimbal responding to a sinusoidal input without the rotor running. The model tracks test data well with regards to phase and timing, but does not match well in velocity amplitude. The model can predict rough order-of-magnitude velocity and position behavior of the gimbal. Gear float, which was not modeled, causes disparities between reality and

the model.

In Section 4.8, a model of the spacecraft simulator was run through a sequence of pointing commands to generate gimbal angle commands. The gimbal angle commands were input to the CMG to evaluate the system's performance under realistic commands. The test was run with both open-loop and PI-controlled configurations. The PI controller degrades performance of the CMG compared to the open-loop results. The PI gains were determined using step inputs, but the simulated maneuver test utilized moving inputs. If a PI controller is to be used operationally, the gains must be chosen based on real commands, such as in the simulated maneuver test (Section 4.8), as opposed to step inputs. The CMG model does not match the real CMG data given the same set of commands because the model design variables were tuned using data from a test that did not have a running rotor. The simulated maneuver test was run with the rotor operating; the model does not match reality due to this incongruity in test conditions. To improve the predictions of the model, it should be re-tuned using data taken from a test in which the rotor is running

The vehicle-level model test (Section 4.9) predicts the effects of CMG gear lash on overall vehicle performance. Gear lash was implemented into a previously built model of the spacecraft simulator. Gear lash was determined to induce a slight time delay on single attitude change maneuvers. However, gear lash has a cumulative time delay effect on sequences of vehicle slews that should be kept in mind when conducting tests. Time delay due to gear lash builds up throughout sequences of maneuvers, which should be accounted for when testing. The model was determined to be not strictly matching to reality because the total angular momentum of the spacecraft/CMG system did not remain constant over time. The incongruity was caused by changing gimbal angles instantaneously without regard for physics within the simulation. The incongruity was found in a previous version of the model (one

without gear lash), so it was determined that the inclusion of gear lash did not cause the error. The model cannot be used to replicate reality exactly, but it can be used to compare parameters within the model, such as gear lash.

5.3 Recommendations for Future Work

5.3.1 Hardware.

Gimbal balance can be improved by designing and installing a more refined mass balance. The balance used for testing used washers as mass increments, which does not allow for fine-tuning of the balance. A better mass balance is under development which allows for adjustment in the radial and axial directions. Such a mass balance is preferable because the system does not depend on small weights to add or take away and can be adjusted quickly.

The gear box on the gimbal motor utilizes three planetary gear trains to step down the speed of the motor in trade for increased torque and finer angular velocity control. The effect of this gear box is that there is a relatively large amount of gear lash in the gimbal assembly. Testing showed that the gear lash would not have a significant effect on response times for the spacecraft simulator, but if the simulator or the CMGs need to meet more stringent requirements or requirements unrelated to response time, the gear box can be changed without the need to design new components. The motor and gear box are inexpensive, therefore replacing them does not represent a significant cost issue.

No testing was performed on the rotor for this research effort. Although the rotor appears to maintain a constant commanded velocity, its measurements were not characterized. The rotor motor Hall sensors can be characterized to smooth the noisy data with a Kalman filter.

Vibration has been an issue with previous iterations of the CMG design mainly

due to the rotor bearings. There is much progress to be made on characterizing the vibrational modes of the rotor and how that affects the bearings. Different styles of bearing and bearing preloads can also be investigated and tested to minimize friction and vibration. Decreasing friction in the rotor bearings would also decrease the power required to start up and operate the CMG, as well as decrease the operating temperature of the rotor.

PID control was tested, but the derivative control was calculated using noisy data. This data can be smoothed out by using a lowpass filter. Retesting with smoother derivative control could open up more possibilities for gimbal control. PID control should also be tested using moving velocity commands, as opposed to step commands. Moving commands would be more representative of the CMG operating conditions; therefore, PID gains derived from such tests would be more applicable than the PID gains calculated in this research. Integrator windup protection should be implemented before further PID testing.

The Kalman filter used in the sensor filtering test (Section 3.4.1) was based on a simple single-state state-space model. The model can be improved by incorporating friction and rotor speed, likely improving the Kalman filter estimates. The residuals and state covariance of the filter were not formally analyzed. In later tests, the residuals were observed to maintain a slight bias, which could be indicative of inaccuracies within the Kalman filter model. However, the tests during which bias were observed were not configured to properly save the Kalman filter data. Further analysis should be performed on the Kalman filter to determine if the estimates can be made more accurate. Improvements in gimbal position and velocity measurements could be realized with further refinement of the Kalman filter.

5.3.2 Models.

The CMG model did not include gyroscopic stiffness dynamics from the rotor, which resulted in inaccurate model results during the model validation test (Section 4.7). Including the rotor in the CMG model would improve the model's ability to replicate reality. A secondary improvement that can be made to the CMG model is to include gear float dynamics. In the current model, the gimbal angle either lags the motor angle (when the gears are engaged) or holds position (when the gears are disengaged). However, there are more subtle dynamics within the interactions of the gears. If the gears were modeled physically, allowing for independent acceleration and impact interactions, then the gear floating observed in Section 4.7 could be replicated. However, before this effort is undertaken, it is recommended that the requirements be determined for how well the CMG model must match the real CMG, because modeling the gear interactions would be time-consuming and such efforts might be better-targeted in other areas of this research.

The spacecraft simulator model violates the law of conservation of angular momentum, making it not representative of reality. Before the model can be used to compare with real test data, the angular momentum conservation condition must be met. This can be corrected by three measures: 1) moving all state changes, including the gear lash function, in the model to within the inner loop (the physical simulation) of the model, 2) shrinking the time step in the integrator, and 3) incorporating singularity avoidance algorithms into the spacecraft model.

Appendix A. Derivation of CMG Equations of Motion

1.1 Spacecraft Dynamics

1.1.1 Kinematics.

The first step in any dynamics study is to define the kinematics of the system. The angular momentum of a body is shown in Eq. (A.1) [37].

$$\vec{H} = I\vec{\omega} \tag{A.1}$$

where \vec{H} is angular momentum, I is the 3x3 MOI matrix, and $\vec{\omega}$ is angular velocity. The angular momentum can be written as the sum of the angular momentum of the spacecraft body and the actuators on-board $\vec{h}_{actuators}$, as shown in Eq. (A.2) [38].

$$\vec{H} = I_{sc}\vec{\omega}_{sc} + \vec{h}_{actuators} \tag{A.2}$$

where the subscript "sc" denotes "spacecraft." Next, we will expand the $\vec{h}_{actuators}$ term, by applying Eq. (A.1) to it. In the case of the CMG, there are two angular rates to account for, the rotor rate Ω and the gimbal rate, $\dot{\delta}$ (Figure 66). The angular momentum of a single CMG is

$$\vec{h}_{CMG}^r = I_g \dot{\delta} \hat{r}_1 + I_r \Omega \hat{r}_3 = \begin{bmatrix} I_g \dot{\delta} \\ 0 \\ I_r \Omega \end{bmatrix}. \tag{A.3}$$

where I_g denotes the MOI of the rotor relative to the gimbal axis (\hat{r}_1 in Figure 66), and I_r denotes the MOI of along the rotor axis (\hat{r}_3 in Figure 66). The superscript "r" denotes that the expression is written in the rotor reference frame. CMGs are generally not mounted to spacecraft such that the gimbal frame aligns with the spacecraft body frame. Therefore, it becomes cumbersome to relate the rotor frame to the

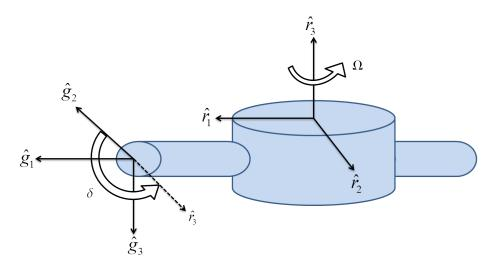


Figure 66. CMG with rotor and gimbal axes

gimbal frame, then the gimbal frame to the body frame. To simplify the derivation, we will discontinue using the gimbal frame, and relate the rotor frame directly to the body frame (Figure 67).

To transform Eq. (A.3) to the body frame, a rotation matrix must be used. A 1-2-3 Euler angle rotation¹ is chosen to rotate the r-frame to the b-frame (Eq. (A.4)).

$$\vec{h}^b = R_3^T(\theta) R_2^T(\beta) R_1^T(\delta) \vec{h}^r \tag{A.4}$$

In order to combine terms more simply later on in the derivation, we will expand the R_2^T and R_1^T terms in Eq. (A.4), then combine the 1- and 2-rotations to yield

$$R_3^T(\theta)R_2^T(\beta)R_1^T(\delta) = R_3^T(\theta) \begin{bmatrix} c\beta & s\beta s\delta & s\beta c\delta \\ 0 & c\delta & -s\delta \\ -s\beta & c\beta s\delta & c\beta c\delta \end{bmatrix}. \tag{A.5}$$

In Eq. (A.5), δ changes with tim, while θ and β are constants. On any given CMG-equipped spacecraft, all CMGs are generally mounted with the same β angle (a.k.a. skew angle), but with different θ angles [17, 32, 33]. Combining Eqs. (A.3)

¹Three consecutive rotations about a body's principal axes.

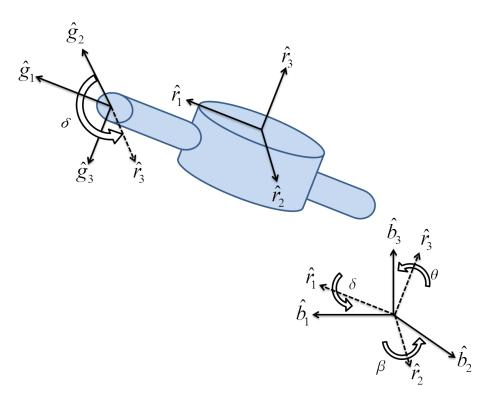


Figure 67. CMG with body frame

and (A.5) gives the following expression for the angular momentum of a CMG in the body frame

$$\vec{h}^b = \begin{bmatrix} c\theta & -s\theta & 0 \\ s\theta & c\theta & 0 \\ 0 & 0 & 1 \end{bmatrix} \begin{bmatrix} I_g c\beta \dot{\delta} + I_r \Omega s\beta c\delta \\ -I_r \Omega s\delta \\ -I_g s\beta \dot{\delta} + I_r \Omega c\beta c\delta \end{bmatrix}. \tag{A.6}$$

where "c" and "s" are sin and cosine functions, respectively. Next, we will incorporate the kinematic equations for a single CMG (Eq. (A.6)) into the equation for a spacecraft. Assuming a spacecraft with only CMGs as attitude actuators, Eq. (A.2) can be rewritten as

$$\vec{H} = I\vec{\omega} + \sum_{j=1}^{n} \vec{h}_j. \tag{A.7}$$

where n denotes the number of CMGs on the spacecraft. Note that, in Eq. A.7, we

have dropped the "sc" subscripts, defining I and ω without subscripts as specific to the spacecraft body. Expanding the h term in Eq. A.7 yields the equation for angular momentum of a spacecraft with n-number of CMGs, assuming the same β angle for all CMGs (Eq. A.8). This is the kinematic expression that describes the angular position and velocity of the spacecraft

$$\vec{H} = I\vec{\omega} + \sum_{j=1}^{n} R_3^T(\theta_j) \begin{bmatrix} I_g c \beta \dot{\delta} + I_r \Omega s \beta c \delta \\ -I_r \Omega s \delta \\ -I_g s \beta \dot{\delta} + I_r \Omega c \beta c \delta \end{bmatrix}.$$
(A.8)

1.1.2 Kinetics.

The relationship between the time-rate of change of angular momentum on a body and the moments acting on the body is defined as [17, 37]

$$\vec{M} = \dot{\vec{H}}.\tag{A.9}$$

Eq. (A.9) is fundamental in attitude dynamics. The time-derivative of Eq. (A.8) must be taken to adapt it to the form of Eq. (A.9) (Eq. (A.10)).

$$\dot{\vec{H}} = I\dot{\vec{\omega}} + \sum_{j=1}^{n} R_{3}^{T}(\theta_{j}) \begin{bmatrix} I_{g}c\beta\ddot{\delta}_{j} - I_{r}\Omega_{j}s\beta s\delta_{j}\dot{\delta}_{j} \\ -I_{r}\Omega_{j}c\delta_{j}\dot{\delta}_{j} \\ -I_{g}s\beta\ddot{\delta}_{j} - I_{r}\Omega_{j}c\beta s\delta_{j}\dot{\delta}_{j} \end{bmatrix} + \vec{\omega} \times I\vec{\omega} + \\
\begin{bmatrix} I_{g}c\beta\ddot{\delta}_{j} - I_{r}\Omega_{j}c\beta s\delta_{j}\dot{\delta}_{j} \\ -I_{g}c\beta\dot{\delta}_{j} + I_{r}\Omega_{j}s\beta c\delta_{j} \\ -I_{r}\Omega_{j}s\delta_{j} \\ -I_{g}s\beta\dot{\delta}_{j} + I_{r}\Omega_{j}c\beta c\delta_{j} \end{bmatrix} \tag{A.10}$$

Some higher order terms can be eliminated from Eq. A.10 if it is assumed that:

A) the gimbal rate is much less than the rotor rate, and B) if the gimbal acceleration is much less than the product of the rotor and gimbal rates (Equations A.11 and A.12). These assumptions are valid because the gimbal rates and acceleration are both generally on the order of one radian per second and one radian per second per second, respectively, and rotor rates are generally on the order of 100 radians per second [15, 17].

$$\dot{\delta} << \Omega \tag{A.11}$$

$$\ddot{\delta} << \Omega \dot{\delta} \tag{A.12}$$

Given the assumptions in Equations A.11 and A.12, Eq. A.10 can be simplified to the governing equation for a spacecraft controlled by a CMG array (Eq. A.13).

$$\dot{\vec{H}} = I\dot{\vec{\omega}} + \sum_{j=1}^{n} R_3^T(\theta_j) \begin{bmatrix} -I_r \Omega_j s \beta s \delta_j \dot{\delta}_j \\ -I_r \Omega_j c \delta_j \dot{\delta}_j \\ -I_r \Omega_j c \beta s \delta_j \dot{\delta}_j \end{bmatrix} + \vec{\omega} \times I\vec{\omega} + \vec{\omega} \times \sum_{j=1}^{n} R_3^T(\theta_j) \begin{bmatrix} I_r \Omega_j s \beta c \delta_j \\ -I_r \Omega_j s \delta_j \\ I_r \Omega_j c \beta c \delta_j \end{bmatrix}$$
(A.13)

Bibliography

- [1] aksIMTM off-axis rotary absolute encoder. Accessed online at http://www.rls.si/en/rls-rotary-and-linear-motion-sensors--15854, 7 April 2014.
 RLS. 2013.
- [2] Sanjay P. Bhat and Pawan K. Tiwari. "Controllability of Spacecraft Attitude Using Control Moment Gyroscopes". In: *IEEE Transactions on Automatic Control* 54.3 (Mar. 2009), pp. 585–590.
- [3] BLWRPG17 Series- Brushless DC Planetary Gearmotos. Accessed online at http://www.anaheimautomation.com/, 1 May 2014. Anaheim Automation.
- [4] BLY17- Brushless Motors. Accessed online at http://www.anaheimautomation.com/, 26 March 2014. Anaheim Automation. 2011.
- [5] Richard Boynton. "Using A Spherical Air Bearing to Simulate Weightlessness". In: 55th Annual Conference of the Society of Allied Weight Engineers (June 1996).
- [6] Avyatar Bukai. "Modeling and Cotnrol of a Four-Axis Control Moment Gyroscope". Bachelor Thesis. Czech Tehnical University in Prague, May 2013.
- [7] Giacomo Como, Sei Zhen Khong, and Magnus Perninge. Nonlinear Control and Servo Systems, Lecture 8, Backlash and Quantization. Course Notes. 2012.
- [8] Goddard Consulting. A Simple Kalman Filter in Simulink. http://www.goddardconsulting.ca/simulink-kalman-filter.html. 2015.
- [9] Ball Aerospace & Technologies Corporation. The Worldview Spacecraft Series. http://www.ballaerospace.com/page.jsp?page=294. 2015.
- [10] Data Sheet MicroAutoBox II 1401/1501. dSpace. 2011.

- [11] Jose A. Dominguez and Bong Wie. "Computation and Visualization of Control Moment Gyroscope Singularities". In: AIAA Guidance, Navigation, and Control Conference and Exhibit (2002).
- [12] Engineers Edge LLC. Ball Bearings ABEC Standard Tolerances Data. http://www.engineersedge.com. 2014.
- [13] Digital Globe. WorldView-3 Data Sheet. Tech. rep. Sept. 2014.
- [14] Chad Greene. Butterworth Filters. http://www.mathworks.com/matlabcentral/fileexchange/38584-butterworth-filters. Accessed: 17-FEB-15. Oct. 2012.
- [15] Charles Gurrisi et al. Space Station Control Moment Gyroscope Lessons Learned. Tech. rep. CP-2010-216272. NASA, 2010.
- [16] Helical Products Company Inc. Flexible Couplings. http://helical.wpengine.com. 2014.
- [17] S. C. Johnson. "Design of a Control Moment Gyroscope Attitude Actuation System for the Attitude Control Subsystem Proving Ground". Wright-Patterson Air Force Base. Masters Thesis. AFIT, 2013.
- [18] Lindsay Kleeman. Understanding and Applying Kalman Filtering. Course Notes. Monash University, Clayton. Accessed January 2015.
- [19] Frederick A. Leve. "Novel Steering and Control Algorithms for Single-Gimbal Control Moment Gyroscopes". PhD thesis. University of Florida, 2010.
- [20] Yun Li, Kiam Heong Ang, and C.Y. Chong. "PID Control System Analysis and Design". In: *IEEE Control Systems Magazine* 26.1 (Feb. 2006), pp. 32–41.
- [21] M50 Control Moment Gyroscope. N61-0096-000-001. Honeywell. P.O. Box 52199, Pheonix, AZ 85072-2199, 2006.

- [22] MathWorks. Backlash documentation page. http://www.mathworks.com/help/simulink/slref/backlash.html?refresh=true. 2015.
- [23] MathWorks. fmincon documentation page. http://www.mathworks.com/help/optim/ug/fmincon.html?refresh=true. 2015.
- [24] Jay McMahon and Hanspeter Schaub. "Simplified Singularity Avoidance Using Variable-Speed Control Moment Gyroscope Null Motion". In: Journal of Guidance, Control, and Dynamics 32.6 (2009), pp. 1938–1943.
- [25] MDC151-050301 Series User's Guide. Anaheim Automation. Sept. 2012.
- [26] NASA. ISS to Date. http://www.nasa.gov/mission_pages/station/structure/isstodate.html. 2011.
- [27] NASA. Outgassing Data for Selecting Spacecraft Materials Online. http://outgassing.nasa.gov/. Accessed: 10-FEB-15. Dec. 2014.
- [28] AFRL/RV: Guidance Navigation and Control Group. Used with permission. Credit: AFRL. 2015.
- [29] Stephen J. O'Neil. *Methods to Minimize Gear Backlash*. http://machinedesign.com/technologies/methods-minimize-gear-backlash. Accessed: 24-JAN-15. Mar. 2002.
- [30] Gruescu Adrian Ovidiu. Sun Fixed. https://grabcad.com/library/sun-fixed-1. Accessed: 17-FEB-15. Apr. 2013.
- [31] Honeybee Robotics. *Microsat Control Moment Gyroscopes*. http://www.honeybeerobotics.com/portfolio/microsat-control-moment-gyroscopes/. Accessed: 5-FEB-15.
- [32] Timothy A. Sands, Jae Jun Kim, and Brij N. Agrawal. "Nonredundant Single-Gimbaled Control Moment Gyroscopes". In: Journal of Guidance, Control, and Dynamics 35.2 (2012), pp. 578–587.

- [33] J. L. Schwartz, M. A. Peck, and C. D. Hall. "Historical Review of Air-Bearing Spacecraft Simulators". In: *Journal of Guidance, Control, and Dynamics* 26.4 (2003), pp. 513–522.
- [34] Honeywel Sensing and Control. *Hall Effect Sensing and Application*. Accessed online, 19 JAN 15, www.honeywell.com. 11 West Spring Street, Freeport, Illinois 61032: Honeywell Inc.
- [35] Steven W. Smith. The Scientist and Engineer's Guide to Digital Signal Processing. 2nd ed. Accessed online, www.analog.com. Californai Technical Publishing, 1999.
- [36] A. Srinath and A C Rao. "Susceptibility of Planetary Gear Trains to Clearances and Misalignments". In: *Indian Journal of Engineering and Materials Sciences* 13 (2006).
- [37] Eric D. Swenson. Intermediate Spacecraft Dynamics, Part 1. Course Notes. 2014.
- [38] Eric D. Swenson. Intermediate Spacecraft Dynamics, Part 12: Reaction Wheels. Course Notes. 2014.
- [39] Conal Watterson. Controller Area Network (CAN) Implementation Guide.

 Tech. rep. Analog Devices Inc., 2012.
- [40] Greg Welch and Gary Bishop. An Introduction to the Kalman Filter. Tech. rep. University of North Carolina at Chapel Hill, 2006.
- [41] James R. Wertz, David F. Everett, and Jeffery J. Puschell. Space Mission Engineering: The New SMAD. 4940 W. 147th Street, Hawthorne, CA 90250: Microcosm Press, 2011.
- [42] Hyungjoo Yoon. "Spacecraft Attitude and Power Control Using Variable Speed Control Moment Gyros". PhD thesis. Georgia Institute of Technology, 2004.

REPORT DOCUMENTATION PAGE

Form Approved OMB No. 0704-0188

The public reporting burden for this collection of information is estimated to average 1 hour per response, including the time for reviewing instructions, searching existing data sources, gathering and maintaining the data needed, and completing and reviewing the collection of information. Send comments regarding this burden estimate or any other aspect of this collection of information, including suggestions for reducing this burden to Department of Defense, Washington Headquarters Services, Directorate for Information Operations and Reports (0704–0188), 1215 Jefferson Davis Highway, Suite 1204, Arlington, VA 22202–4302. Respondents should be aware that notwithstanding any other provision of law, no person shall be subject to any penalty for failing to comply with a collection of information if it does not display a currently valid OMB control number. PLEASE DO NOT RETURN YOUR FORM TO THE ABOVE ADDRESS.

1. REPORT DATE (DD-MM-YYYY) 2. REPORT TYPE			3. DATES COVERED (From — To)	
06-03-2015	Master's Thesis		Sept 2013 — Mar 2015	
4. TITLE AND SUBTITLE		5a. CON	TRACT NUMBER	
Characterization and Modeling of a Control Moment Gyroscope			5b. GRANT NUMBER	
		5c. PRO	GRAM ELEMENT NUMBER	
6. AUTHOR(S)		5d. PRO	JECT NUMBER	
Penn, Dylan R, 2d Lt, USAF		5e. TASK NUMBER		
		5f. WOR	K UNIT NUMBER	
7. PERFORMING ORGANIZATION NAME(S) AND ADDRESS(ES) Air Force Institute of Technology Graduate School of Aeronautical and Astronautical Engineering (AFIT/E		ENY)	8. PERFORMING ORGANIZATION REPORT NUMBER	
2950 Hobson Way WPAFB OH 45433-7765 (937) 255-3636, x7479			AFIT-ENY-MS-15-M-235	
9. SPONSORING / MONITORING AGENCY NAME(S) AND ADDRESS(ES)			10. SPONSOR/MONITOR'S ACRONYM(S)	
Air Force Research Laboratory, Space Vehicles Directorate, Guidance, Navigation, and Control Group			AFRL/RVSV	
3550 Aberdeen Ave SE Kirtland AFB NM 87117 COMM 505-853-7476			11. SPONSOR/MONITOR'S REPORT NUMBER(S)	
Email: frederick.leve@us.af.mil 12. DISTRIBUTION / AVAILABILITY				
DISTRIBUTION STATEMENT APPROVED FOR PUBLIC RE	A: LEASE; DISTRIBUTION UNLIMITED			

13. SUPPLEMENTARY NOTES

This work is declared a work of the U.S. Government and is not subject to copyright protection in the United States.

14. ABSTRACT

The Air Force Research Laboratory (AFRL) is developing a spacecraft simulator that uses Control Moment Gyroscopes (CMGs). Prior to the research herin, the Air Force Institute of Technology (AFIT) designed and built six laboratory-rated CMGs for use on the AFRL spacecraft simulator. The main contributions of this research are in the testing and modeling of a single CMG.

Designing, building, and operating spacecraft simulators is time consuming and expensive, but less so than tests with on-orbit spacecraft. Reductions in cost and schedule can be realized by investing in modeling the spacecraft simulator and payload before testing. A model of the spacecraft simulator was created in previous research efforts, but was an ideal model; it did not include dynamics based on real CMGs. The objective of this research is to characterize and model a single CMG to determine the effects the real CMG's performance will have on the performance of the AFRL spacecraft simulator.

model a single CMG to determine the effects the real CMG's performance will have on the performance of the AFRL spacecraft simulator. The gimbal motor utilizes a planetary gearbox, which has gear lash of 5°. Gear lash makes the existence of gravitational disturbance torques noticeable in the gimbal angular position measurements. An analytical model of the CMG gimbal was created in MATLAB. The model predicts the nonlinear dynamic behavior of the real CMG.

A model of the spacecraft simulator was run through a sequence of pointing commands to generate gimbal angle commands which were then used to command the CMG to evaluate the system's performance under realistic conditions. Gear slack has a cumulative time delay effect on vehicle slew responses of approximately one second over five maneuvers. The results of the tests performed in this thesis can be used to predict performance of CMG and spacecraft simulator behavior.

15. SUBJECT TERMS

Control Moment Gyroscope, Attitude Controls, Gear Lash, Spacecraft Simulator

16. SECURITY CLASSIFICATION OF:				19a. NAME OF RESPONSIBLE PERSON	
a. REPORT	b. ABSTRACT	c. THIS PAGE	ABSTRACT	PAGES	Dr. Eric Swenson, AFIT/ENY
U	U	U	U	120	19b. TELEPHONE NUMBER (include area code) (937) 255-3636, x7479; eric.swenson@afit.edu